Instabilities and vortex dynamics in shear flow of magnetized plasmas

T. Tajima, W. Horton, P. J. Morrison, J. Schutkeker, T. Kamimura, K. Mima, and Y. Abe
Institute for Fusion Studies, The University of Texas at Austin, Austin, Texas 78712

(Received 19 March 1990; accepted 1 November 1990)

Gradient-driven instabilities and the subsequent nonlinear evolution of generated vortices in sheared $\mathbf{E}\times\mathbf{B}$ flows are investigated for magnetized plasmas with and without gravity (magnetic curvature) and magnetic shear by using theory and implicit particle simulations. In the linear eigenmode analysis, the instabilities considered are the Kelvin–Helmholtz (K–H) instability and the resistive interchange instability. The presence of the shear flow can stabilize these instabilities. The dynamics of the K–H instability and the vortex dynamics can be uniformly described by the initial flow pattern with a vorticity localization parameter ϵ. The observed growth of the K–H modes is exponential in time for linearly unstable modes, secular for the marginal mode, and absent until driven nonlinearly for linearly stable modes. The distance between two vortex centers experiences rapid merging while the angle θ between the axis of the vortices and the external shear flow increases. These vortices proceed toward their overall coalescence, while shedding small-scale vortices and waves. The main features of vortex dynamics, the nonlinear coalescence and the tilt or the rotational instabilities of vortices, are shown to be given by using a low-dimension Hamiltonian representation for interacting vortex cores in the shear flow.

I. INTRODUCTION

The presence of shear in the flow of neutral fluids and plasmas gives rise not only to instability of the sheared layer, i.e., the Kelvin–Helmholtz (K–H) instability, but also to stabilization of other instabilities, the interchange mode [Rayleigh–Taylor (R–T) instability], for instance. Resistive-interchange-driven turbulence has been proposed as a mechanism for the anomalous thermal transport in stellarators and in edge plasmas of tokamaks. Recent calculations indicate that a strong nonuniform radial electric field can suppress the interchange[1] and resistive pressure-gradient-driven instabilities.[2] The fluid dynamics of shear flows under the influence of gravity is also important for the problem of an imploding inertially confined plasma. In the initial phase of implosion, short-wavelength modes are stabilized by the ablative flow and relatively long-wavelength modes can grow on an ablation surface.[3,4] Large-scale vortices excited by the R–T instability are adiabatically compressed, and thus increase in strength during the implosion. It appears that the shear flows associated with large-scale-length vortices suppress the short-wavelength R–T mode in the stagnation phase that occurs during the final phase of the implosion. The presence of vortices can also influence the nature of turbulence and associated transport. In the isotropic two-dimensional (2-D) Navier–Stokes turbulence the well-known Kolmogorov power spectrum of k^{-3} developed from space filling small-scale eddies. However, we find that the turbulence power spectrum changes to a steeper power law in k in the presence of vortical structure in the fluid in the wave number regime on the scale of the vortices. Thus the presence and dynamics of the vortices may strongly affect the macroscopic behavior of turbulence.

In this work, we extend the previous work[5] by investigating the shear flow effects on the gravitational instability and the magnetic shear effects on the K–H and R–T instabilities. Also, the detailed analysis of the nonlinear evolution of large size vortices is presented here.

In magnetic confinement devices the shear flow occurs at the boundary between the rotating core plasma and the wall or limiter. The magnitude and direction of the core rotation is determined by the strength of the nonambipolar loss rates leading to the charge-up of the plasma. The mirror or open field line confinement system has an intrinsically faster electron loss rate leading to the net positive potential of several times the electron temperature. In the stellarator with strong electron cyclotron heating there is also a dominant electron loss and positive charge to the plasma. In contrast, for stellarators with neutral beam injection or ion cyclotron heating and, in general, for tokamaks, there is a net radial ion loss rate from finite ion orbits size effects and the plasmas build up a substantial, of order the ion temperature, negative potential. The positive potential plasmas rotates in the ion diamagnetic direction and the negative potential plasmas in the electron diamagnetic direction. In typical stability analysis the assumption is made that the rotation is sufficiently close to a solid body rotation and sufficiently slow that the only effect is to Doppler shift the wave frequencies from the values calculated in the absence of rotation. The conditions for the limit of this approximation are given in Ref. 1 for the rotating cylindrical plasma with ω_{*e} and ω_{*i} drift modes. In the presence of shear flow we can estimate the condition for a strong effect of the shear flow on a mode of growth rate γ_{k_y}, wave number k_y, and the mode width Δx by the condition

$$k_y \, \Delta x \, u' > \gamma_{k_y}.$$

 0899-8221/91/040938-17$02.00

Here, we consider a configuration of plasma density, shear flow, and magnetic shear as shown in Fig. 1, where $u' = u/a$. Applying this condition to the values of k, Δx, and γ_k for the interchange, resistive g, and the drift wave, gives a first estimate for the shear flow required to reduce the growth rate. Table I shows the condition on u' obtained from this criterion for several forms of plasma turbulence.

Since the sheared velocity flow contains a source of free energy, one expects instability to arise from the shear flow, which it does above a critical strength. However, the forms of the eigenmodes of the K–H are sufficiently different from those of the interchange-drift-wave-type of instability that there is generally a substantial window between the stabilizing effect of the shear flow on the interchange modes and the onset of the Kelvin–Helmholtz instability, as shown in some detail for the $m = 1$ and 2 modes of the rotating cylinder in Ref. 1.

Recent experiments[6] in the DIII-D tokamak show that associated with L (low) to H (high) confinement mode transition, there is a substantial increase in the perpendicular component of the plasma flow velocity, as measured by the spectroscopic shifts of helium line radiation.[7] No such appreciable change is observed in the toroidal component of the plasma flow velocity. Taylor *et al.*[8] also report no appreciable change in the toroidal velocity and a substantial increase in the poloidal velocity with the onset of H-mode-like plasma conditions. The abrupt change in the flow speed is interpreted to be due to a strengthening of the radial electric field strength. Shaing and Crume[9] have interpreted this change in the radial field strength with increased nonambipolar radial ion currents and a bifurcation to a new rotational equilibrium.

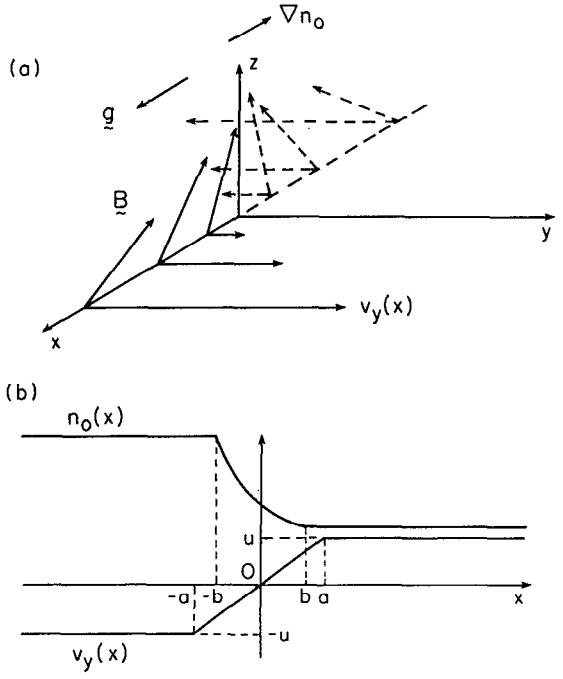

FIG. 1. (a) Slab geometry showing coordinates used to describe the sheared magnetic field $\mathbf{B}(x)$ and sheared flow velocity $v_y(x)$ along with the directions of ∇n_0 and $\mathbf{g}$. (b) The piecewise continuous profiles of the sheared flow velocity $v_y(x)$ and the density $n_0(x)$.

Shaing *et al.*[2] note that without considering the stability problem there may arise improved confinement resulting from the shear flow layer. Biglari *et al.*[10] also discuss that the shear flow in itself may reduce the transport. A simple single-mode description of the shear flow reduction in transport is given by the convective cell island width formula[1]

$$\Delta r = 2\left(\frac{c\tilde{\varphi}}{rB\,|d\Omega/dr|}\right)^{1/2},$$

which traps plasma to form an insulating layer. Here Ω is the poloidal rotation rate $\Omega = (c/rB)(d\Phi/dr)$ and $\tilde{\varphi}$ is the amplitude of the vortex wave.

In the present work we consider how the shear flow may strongly modify the strength of the growth rates of the underlying turbulence generation from the interchange- and drift-wave-types of instabilities in the limit of ion gyroradius small compared with all scale lengths, both in theory and simulation. Theilhaber and Birdsall[11] studied the K–H instability with finite Larmor radius effects fully taken into account but without magnetic shear effect.

A similar charge separation induced shear flow appears in the barium ion injection in the ionosphere.[12] Other magnetospheric appearances[13] and astrophysical ones such as jets[14] of the shear flow instability are noted. When the shear flow is sufficiently strong to dominate the stabilizing effects of magnetic shear, the growth rate reaches a maximum for wave number $k_y \simeq 1/2a$, where the maximum growth rate is $\gamma_{\max} \simeq 0.2 \max|dv_y/dx| \simeq 0.2u/a$. Since the short-wavelength modes with $k_y a > 1$ are stable to exponential growth, vortices excited by the K–H instability extend over all the shear flow region with $\lambda_x \sim \lambda_y > a$. When the shear flow dominates, the density and temperature fields are passively convected with the fluctuations characterized by $e\varphi/T_e \gg \delta n/n$, $\delta T/T$.

The fastest growing normal mode forms a perturbed vortical flow pattern with the axis of the vortex tilted with respect to the flow direction, as shown by theory[1] and simulation.[5] The tilting of the vortical flow produces a momentum flux $\pi = \langle v_x v_y \rangle$ across the shear layer. The momentum flux takes energy out of the shear and puts it into the vortical flows. Subsequently the vortices coalesce, with the dominant wavelength shifting to a multiple of the original wavelength. This shifting to longer wavelengths is a configuration space representation of the inverse cascade. Often the coalescing vortices or islands persist for long times.

The effect of the electron parallel motion on stabilization of the K–H mode is shown to reduce the maximum growth rate. The electron density fluctuations induced by the electron parallel motion ($\nabla_\parallel \cdot \mathbf{j}_\parallel$) balance with ion density fluctuations generated by the ion perpendicular motion ($\nabla_\perp \cdot \mathbf{j}_\perp$). Namely, for charge neutral currents we have

$$\nabla_\perp \cdot \mathbf{j}_\perp + \nabla_\parallel \cdot \mathbf{j}_\parallel = 0.$$

Since $j_\parallel \sim \eta E_\parallel = -ne^2 \nabla_\parallel \phi / m\nu_{ei}$, $\mathbf{j}_\perp \sim -(d/dt) \times (ne\nabla_\perp \phi / B\omega_{ci})$ from the ion inertia current. The effect of the electron parallel motion is significant when

$$k_\parallel^2 v_e^2 / \nu_{ei} \gtrsim k_\perp^3 u \rho_s^2.$$

Here ν_e is the electron thermal velocity, ν_{ei} is the electron–ion collision frequency, ϕ is the fluctuation potential, ω_{ci} is

TABLE I. Effect of shear flow on other instabilities.

Mode	Characteristics		Shear flow condition
	$k_y\Delta x$	γ_{k_y}	$k_y\Delta x u' > \gamma_{k_y}$
Rayleigh–Taylor	1	$\gamma_0 = \left(\frac{g}{L_n}\right)^{1/2}$	$u' > \left(\frac{g}{L_n}\right)^{1/2}$
Resistive g	$\left(\frac{c^2\eta k_y^2}{4\pi\gamma_k}\right)^{1/2}$	$\gamma_{k_y} = \left(\frac{c^2\eta k_y^2}{4\pi}\right)^{1/3}\gamma_0^{2/3} > \lvert\omega_*\rvert$	$u' > \left(\frac{g}{L_n}\right)^{1/2}$
Eta i	$k_y\rho_s\left(\frac{L_s}{L_n}\right)^{1/2}$	$\lvert\omega_*\rvert\frac{r_n}{L_s}(\eta_i-\eta_c)$; $k_y\rho_s \ll K_\parallel^{-1/2}$	$u' > \frac{c_s}{L_s}\left(\frac{L_n}{L_s}\right)^{1/2}(\eta_i-\eta_c)$
$\eta_i = \frac{d\ln T}{d\ln n}$; η_c (threshold)		$\lvert\omega_*\rvert\left(\frac{r_n}{L_s}(\eta_i-\eta_c)\right)^{1/2}$; $k_y\rho_s \simeq K_\parallel^{-1/2}$	$u' > \frac{c_s}{L_s}(\eta_i-\eta_c)^{1/2}$
Collisional drive wave	$\left(\frac{L_s^2}{l_e L_m}\right)^{1/2}$	$\gamma_k \lesssim \lvert\omega_{*e}\rvert \lesssim \frac{c_s}{L_n}$	$u' > \frac{c_s}{(L_n L_s)^{1/2}}\left(\frac{l_e}{L_s}\right)^{1/2}\left(\frac{m_i}{m_e}\right)^{1/4}$
$k_\parallel^2 v_e^2 \sim \omega_* \nu_e$ $l_e = \frac{v_e}{\nu_e}$			
Dissipative trapped electron mode			
$\varepsilon = \frac{r}{R}$	$k_y\rho_s\left(\frac{L_s}{L_n}\right)^{1/2}$	$\gamma_k \simeq \frac{\varepsilon^{3/2}\omega_*^2\eta_e}{\nu_e} \lesssim \lvert\omega_{*e}\rvert$	$u' > \left(\frac{r}{R}\right)^{3/2}\left(\frac{L_n}{L_s}\right)^{1/2}\frac{c_s^2}{\nu_e L_n L_{T_e}}$

the ion cyclotron frequency, ρ_s is the hybrid ion gyroradius given by $\rho_s = c(m_i T_e)^{1/2}/eB$, and $2u$ is the velocity shear limits in the $E\times B$ drift velocity. For a K–H mode with $k_\perp \lesssim 1/a$ the critical tilt angle θ_c, as measured between the k vector and the ambient magnetic field, is given by $\theta_c \simeq (\rho_s/a)[(u/v_e)/(a/l_e)]^{1/2}$, where l_e is the mean-free path of electrons. For $\theta \gtrsim \theta_c$, the K–H instability will be stabilized. In the case of a sheared magnetic field, the tilt angle $\theta \simeq a/L_s$ is produced by the shearing of the magnetic field, will L_s the shear length. Therefore the K–H mode is significantly stabilized when $L_s \lesssim (a^2/\rho_s)(l_e v_e/ua)^{1/2}$. The ratio of the parallel diffusion $k_\parallel^2 v_e^2/\nu_{ei}$ to the ion inertial acceleration $k_\perp^2\rho_s^2 k_y u$ is sometimes called R, as is given by $R = k_y v_e^2 a^4/\nu_{ei} u\rho_s^2 L_s^2$. Both the resistive g and the K–H growth rates decrease with increasing R.

When there exist a density gradient and a gravity force as shown in Fig. 1, the interchange modes can be unstable. Here we use gravity to represent either the effective acceleration from the ∇B curvature drift of the ions or the acceleration during implosion. The maximum growth rate for the density gradient $d\ln n_0/dx \equiv -1/L_n$ and the gravity $g \simeq v_i^2/R$, where v_i is the ion thermal velocity and R the major radius of tokamak, is $\sqrt{g/L_n}$.

When there is a shear flow with $\lvert dv_y/dx\rvert \simeq u/a$, the interchange mode can be stabilized. Stabilization by the velocity shear occurs when $u/a > \sqrt{g/L_n}$. This is related to the critical Richardson number.

Let us give two examples of the above instabilities. The first example is an edge plasma of the TEXT tokamak.[15] The shear flow layer width $2a \sim 0.6$ cm, in which the velocity u changes from -3×10^5 to 3×10^5 cm/sec, the electron temperature $T_e \simeq 20$ eV, the density $n_0 \simeq 1$–$2\times10^{12}/\text{cm}^3$, the density scale length $L_n \simeq 1$ cm, and the magnetic field curvature $R \gtrsim 1$ m. The electron mean-free path $l_e \sim 200$ cm and the hybrid ion gyroradius $\rho_s \simeq 0.02$ cm for the above parameters. The K–H modes in this case are stabilized when the shear length $L_s \lesssim a(2.7 v_e l_e a/u\rho_s^2)^{1/2} \lesssim 50$ m. As for the interchange instability, the flute mode is stabilized by the strong shear flow, since $u/a \simeq 10^6/\text{sec} \gtrsim \sqrt{g/L_n} \simeq 5\times10^5/\text{sec}$.

The second example is the Rayleigh–Taylor instability of the imploded laser plasma. A typical acceleration rate gives $g \simeq c_s^2/\Delta R$ for the target shell thickness ΔR. The velocity shear will be given by $\alpha c_s/\Delta R$. Since the Rayleigh–Taylor mode growth rate is $\sqrt{kg}$, the stability criteria is roughly given by

$$\alpha c_s/\Delta R \gtrsim 2\sqrt{kc_s^2/\Delta R}\,.$$

Therefore the unstable modes are limited to short wavelengths where $k \lesssim \alpha^2/4\,\Delta R$, and $\alpha \gtrsim 1$ will strongly stabilize the Rayleigh–Taylor instability.

The characteristic time scale of the Kelvin–Helmholtz or interchange processes do not involve a characteristic oscillation frequency, such as the plasma, cyclotron, or the ion acoustic frequencies, in the center of mass frame of the plasma. The plasma flow is due to the $E\times B$ drift of the guiding centers and the characteristic time scales are those of hydrodynamic flows, although the elementary process is that of a magnetized plasma with long range Coulomb interactions. The effects of finite pressure density gradient and gravity, across the magnetic field and the shear flow layer, bring in the drift wave frequencies ω_{*e} and ω_{*pi}. Thus to study the nonlinear evolution of shear flows and vortices associated with the magnetized plasma through numerical simulation, time scales much longer than the plasma oscillation periods are required. We employ the implicit particle simulation technique with the decentering algorithm,[16] which systematically removes the characteristic time scales and spatial

length scales that are smaller than the time step Δt and space scales Δx chosen for the space-time grid. The filtering method has been shown to preserve the accuracy for the low-frequency ($\omega \Delta t \ll 1$) dynamics.[17]

In the present paper we investigate the nonlinear evolutions of the Kelvin–Helmholtz and interchange instabilities as an initial value problem through particle simulation, in contrast to the previous work,[5] where the shear flow was externally fixed with an imposed driver, as would arise from nonambipolar losses in the background plasma. Namely, in the present simulation, we assume that a space-charge separation exists initially, which produces an initial $E \times B$ shear flow. Note that any processes that induce charge separation have not been included in the simulation. The secular growth and decay of the marginally stable normal modes are also studied. After the linear stage of exponential growth of the primary normal modes, the growth of secondary modes can be nonlinearly triggered.

In order to systematically explore the parametric dependence of the development in the nonlinear stage, we isolate the evolution of vortex coalescence and associated processes caused by vortex formation, which in turn is due to the K–H instability and its nonlinear evolution. To investigate the second stage, the system is initiated from the secondary equilibrium of a chain of finite-amplitude vortices. The chain of vortices is unstable against the coalescence mode and against the tilt or rotational mode. In this nonlinear regime the growth of coalescence and tilt modes are nonlinear instabilities showing the finite time singularity like $(t_c - t)^{-\alpha}$ for times $t \lesssim t_c$.

In Sec. II the equations for K–H and interchange instabilities, both for plasmas with and without a magnetic field are derived. These equations include the effects of velocity shear, magnetic shear, density gradients, gravity, and electron–ion collisions. The linear dispersion relations derived from the equations for the two instabilities are also discussed in two analytic limits. In Sec. III we study the initial value simulation of the shear flow K–H instabilities, both in its linear and nonlinear stages. In Sec. IV the nonlinear evolution of vortices, starting from the periodic chain of vortices, is examined and the coalescence and tilt instabilities of vortices are studied via the particle simulation method as well as theoretical modeling. In Sec. V we summarize the results and discuss the applications of the results to fusion plasmas.

II. VORTEX EQUATION IN A PLASMA WITH VELOCITY SHEAR, MAGNETIC SHEAR, GRAVITY, AND DENSITY GRADIENT: K–H AND INTERCHANGE STABILITY ANALYSIS

We carry out linear theoretical analysis of plasma stability associated with shear flows. We consider the effects of shear flows and gravity both in magnetized and unmagnetized plasmas. In the case of a magnetized plasma, the static sheared magnetic field is given by $\mathbf{B} = B_0(\hat{\mathbf{z}} + \hat{\mathbf{y}}x/L_s)$, which is shown in Fig. 1. The initial ion density has a gradient of $1/L_n = -\partial \ln n_0/\partial x$ between $x = b$ and $-b$. The flow velocity is in the y direction, and changes according to

$$\mathbf{v}^0 = \begin{cases} u, & x > a, \\ u(x/a), & |x| \leqslant a, \\ -u, & x < -a. \end{cases}$$

The configuration is schematically shown in Figs. 1(a) and 1(b). Except for especially indicated cases, we consider the previous plasma configuration. Also, gravity is applied in the x direction, which destabilizes (stabilizes) the interchange mode for $\gamma_g^2 = g/L_n \gtrless 0$.

In the case of low-frequency modes with relatively long wavelengths $\lambda \gg \lambda_{De}$ and ρ_i, where λ_{De} and ρ_i is the electron Debye length and the ion Larmor radius, the wave dynamics can be analyzed by fluid equation for electron and ion, and the condition of charge neutrality can be assumed. Namely,

$$n_i = n_e = n. \tag{1}$$

From the electron equation of motion along $\mathbf{B}$, we obtain the equation for the parallel electron current $j_\parallel$,

$$m_e\left(\frac{\partial}{\partial t} + \mathbf{v}_E \cdot \nabla\right) j_\parallel = -ne^2 \nabla_\parallel \phi + e\nabla_\parallel p_e - m_e \nu_{ei} j_\parallel \simeq 0, \tag{2}$$

where $\mathbf{v}_E$ is the $\mathbf{E}\times\mathbf{B}$ drift, ϕ is the electrostatic potential perturbation, p_e is the electron pressure, and ν_{ei} is the effective electron collision frequency. Using the electron equation of continuity and Eq. (2), we obtain

$$\left(\frac{\partial}{\partial t} + \mathbf{v}_E \cdot \nabla_\perp\right) n_e = \frac{1}{e}\nabla_\parallel \cdot \mathbf{j}_\parallel = \frac{1}{m\nu_{ei}}(-n_0 e \nabla_\parallel^2 \phi + \nabla_\parallel^2 p_e). \tag{3}$$

Assuming T_e constant and $n_e = n_0(x)(1 + \tilde{n}_e)$, Eq. (3) is rewritten as

$$\left(\frac{\partial}{\partial t} + \mathbf{v}_E \cdot \nabla\right)\tilde{n}_e = -\frac{c_s \rho_s}{L_n}\frac{\partial \tilde{\phi}}{\partial y} + \frac{v_c^2}{\nu_{ei}}\nabla_\parallel^2(\tilde{n}_e - \tilde{\phi}), \tag{4}$$

where $\tilde{\phi} = e\phi/T_e$, $L_n = |d \ln n_0/dx|^{-1}$, $c_s = \sqrt{T_e/M_i}$, and the ion hybrid gyroradius $\rho_s = c_s/\omega_{ci}$, where ω_{ci} is the ion cyclotron frequency. In Eq. (4), nonlinearities other than the nonlinear polarization drift are neglected.

From the ion equation of motion, we obtain $\mathbf{v}_{i\perp}$, the ion drift velocity perpendicular to the magnetic field

$$\mathbf{v}_{i\perp} = \mathbf{v}_E + \mathbf{v}_g + \mathbf{v}_d + \mathbf{v}_p, \tag{5}$$

where

$$\mathbf{v}_E = \{[\mathbf{z} \times \nabla(\phi_0 + \phi)]/B_0\}c, \tag{6}$$

$$\mathbf{v}_g = -(g/\omega_{ci})\hat{\mathbf{y}}, \tag{7}$$

$$\mathbf{v}_d = [(\hat{\mathbf{z}} \times \nabla p_i)/neB_0]c, \tag{8}$$

and

$$\mathbf{v}_p = -\left(\frac{\partial}{\partial t} + (\mathbf{v}_E + \mathbf{v}_g)\cdot\nabla_\perp\right)\frac{\nabla_\perp(\phi_0 + \phi)}{\omega_{ci}B_0}c. \tag{9}$$

Here ϕ_0 is a background plasma potential. Note here that when finite ion Larmor radius is included, the convective derivative of Eq. (9) may be replaced by $(\mathbf{v}_E + \mathbf{v}_d + \mathbf{v}_g)\cdot\nabla$, as discussed in Refs. 18 and 19. The ion equation of continuity and Eq. (5) imply

$$\left(\frac{\partial}{\partial t}+(\mathbf{v}_E+\mathbf{v}_g)\cdot\nabla_\perp\right)n_i-\rho_s^2\nabla_\perp \cdot\left[n_i\left(\frac{\partial}{\partial t}+(\mathbf{v}_E+\mathbf{v}_g)\cdot\nabla_\perp\right)\nabla_\perp(\tilde{\phi}+\tilde{\phi}_0)\right]=0. \tag{10}$$

Setting $n_i=n_0(x)(1+\tilde{n}_i)$, using $\tilde{\mathbf{v}}_E=[(\hat{z}\times\nabla\tilde{\phi})/B_0]c$, and defining

$$v_0=\frac{c}{B_0}\frac{\partial\phi_0}{\partial x}-\frac{g}{\omega_{ci}}, \tag{11}$$

which is the ambient ion flow velocity, Eq. (10) yields,

$$\left(\frac{\partial}{\partial t}+(\mathbf{v}_E+\mathbf{v}_g)\cdot\nabla_\perp\right)\left(\tilde{n}_i-\frac{1}{n_0}\rho_s^2\nabla_\perp\cdot n_0\nabla_\perp\tilde{\phi}\right) =-\rho_s^2 v_0''\frac{\partial\tilde{\phi}}{\partial y}-\frac{c_s\rho_s}{L_n}\frac{\partial\tilde{\phi}}{\partial y}+\frac{\rho_s^2}{L_n}v_0'\frac{\partial\tilde{\phi}}{\partial y}, \tag{12}$$

where the prime indicates d/dx. Equations (4), (12), and the charge neutrality condition of Eq. (1) are our basic equations. Note that only the dominant nonlinearity is retained in Eq. (12), as in Eq. (4). When we linearize Eqs. (4) and (12) and set $v_g=0$ and $\nabla_\parallel=0$, Eqs. (16) and (12) can be reduced to Eq. (31) of Ref. 11 and Eq. (7.17) in Chap. 7 of Mikhailovski[18] and to the Rosenbluth–Simon equation.[19]

In the absence of the gravitational drift velocity and for a uniform $\mathbf{v}_E$ the coupled equations (4) and (12) reduce to the well-known Hasegawa–Wakatani equations[20] describing the collisional drift wave. In the low collisionality-strong shear limit $k_\parallel^2 v_e^2>\nu_{ei}|\omega_k|$ the density is forced to be close to the local Boltzmann distribution and the equations reduce to the single dissipative equation[21] often used to study drift wave turbulence. Including the gravitational acceleration g/L_n gives the resistive g mode for the collision dominated plasma and an additional stabilizing or destabilizing effect to the drift wave in the weak collisionality regime.

Let us look at a linearized wave equation for a mode that varies as $\tilde{\phi}(x)\exp[-i\omega t+iky+ik_\parallel(x)z]$, where $k_\parallel(x)=kx/L_s$. Eliminating $\tilde{n}=\tilde{n}_i=\tilde{n}_e$ from Eqs. (4) and (12), we obtain

$$\frac{1}{n_0}\rho_s^2\frac{d}{dx}\left(n_0\frac{d}{dx}\tilde{\phi}\right)=\left(\rho_s^2k^2-\frac{\rho_s^2k(v_0''-v_0'/L_n)}{\omega-kv_0}-\frac{(kv_g+ik_\parallel^2D_\parallel)(k\rho_sc_s/L_n)}{(\omega-kv_0)(\omega-kv_{E0}+ik_\parallel^2D_\parallel)}+\frac{ik_\parallel^2D_\parallel}{\omega-kv_{E0}+ik_\parallel^2D_\parallel}\right)\tilde{\phi}, \tag{13}$$

where $D_\parallel=v_e^2/\nu_{ei}$ is the parallel electron diffusion coefficient and $v_{E0}=c\,\partial\phi_0/\partial x\,B$. Equation (13) includes various MHD instabilities driven by gravity, shear flow, and density gradient, which correspond to interchange instability, Kelvin–Helmholtz instability, resistive g mode, and drift wave instabilities. In the following discussion, shear flow stabilization of the interchange mode is investigated.

We derive dispersion relations for the following two cases. Case 1 is the discontinuous density step: $b\to0$, $n_0=n_1$, for $x>0$, $n_0=n_2$ for $x<0$, $U/a=$ const as $a\to\infty$ and no magnetic shear ($L_s\to\infty$). Case 2 is the smooth density change: $a=b$ and $n_0(x)=n_0\exp(x/L_n)$ for $|x|<b$, and $L_s\to\infty$.

A. Case 1. Discontinuous density step

Setting $v_0''=0$, a solution of Eq. (13) is written as follows:

$$\tilde{\phi}=Ae^{-kx},\quad x>0,$$

and

$$\tilde{\phi}=De^{kx},\quad x<0.$$

The jump conditions at $x=0$ are

$$A=D \tag{14}$$

and

$$\rho_s^2\left(n_1\frac{d\tilde{\phi}}{dx}\bigg|_{x=+0}-n_2\frac{d\tilde{\phi}}{dx}\bigg|_{x=-0}\right)=k\frac{(n_2-n_1)v_0'\rho_s^2}{\omega-kv_g}\tilde{\phi}+\frac{\rho_sk^2v_gc_s(n_1-n_2)}{\omega(\omega-kv_g)}\tilde{\phi}. \tag{15}$$

Using Eqs. (14) and (15), the dispersion relation is written as

$$\omega(\omega-kv_g)-\alpha(u/a)(\omega-kv_g)+\alpha kg=0, \tag{16}$$

which yields

$$\omega=\frac{1}{2}\left(kv_g+\frac{\alpha u}{a}\right)\pm\frac{1}{2}\sqrt{\left(kv_g+\frac{\alpha u}{a}\right)^2-4\alpha kg}, \tag{17}$$

where $\alpha=(n_1-n_2)/(n_1+n_2)$ is the Atwood number. The interchange mode is unstable when $2\sqrt{\alpha kg}\geqslant|\alpha u/a+kv_g|$. Hence the interchange process is stabilized by the shear flow when

$$\sqrt{\alpha}(u/2a)\geqslant\sqrt{kg}. \tag{18}$$

B. Case 2. Smooth density change

Here $a=b$ and $n_0(x)=n_0\exp(-x/L_n)$ for $|x|<a$ and $k_\parallel=kx/L_s$, as shown in Fig. 1. The eigenmode is

$$\tilde{\phi}=\begin{cases}A\exp\left(\int_a^x\kappa_1\,dx\right), & \text{for } x>a,\\ B\exp\left(\int_a^x\kappa_1\,dx\right)+C\exp\left(\int_{-a}^x\kappa_2\,dx\right), & \text{for } |x|<a,\\ D\exp\left(\int_{-a}^x\kappa_2\,dx\right), & \text{for } x<0,\end{cases} \tag{19}$$

where the Wentzel–Kramers–Brillouin (WKB) approximation has been used in writing Eq. (19). The validity of the approximation is discussed later. In Eq. (19), $\kappa_1=+1/2L_n-q$, $\kappa_2=+1/2L_n+q$,

$$q(x)=\left(\frac{1}{4L_n^2}+k^2+\frac{kv_0/L_na}{\omega-kv_0}-\frac{(kv_g+iv)kc_s}{(\omega-kv_0)(\omega-kv_{E0}+iv)L_n\rho_s}+\frac{iv/\rho_s^2}{\omega-kv_{E0}+iv}\right)^{1/2}, \tag{20}$$

$\nu = k_\parallel^2 D_\parallel$, and we assume $\mathrm{Re}\,\kappa_1 < 0$ and $\mathrm{Re}\,\kappa_2 > 0$. The jump conditions are

$$A = B + Ce^{\psi_2},$$
$$D = Be^{-\psi_1} + C, \tag{21}$$

and

$$\kappa_1'(a)A - \kappa_1(a)B - \kappa_2(a)Ce^{\psi_2} = -\frac{ku/a}{\omega + ku - kv_g}A,$$
$$\kappa_1(-a)Be^{-\psi_1} + \kappa_2(-a)C - \kappa_2'(-a)D = +\frac{ku/a}{\omega - ku - kv_g}D. \tag{22}$$

Here $\psi_{1,2} = \int_{-a}^{a}\kappa_{1,2}(x)dx$. Equations (21) and (22) yield the dispersion relation

$$\left(\kappa_1'(a) - \kappa_1(a) - \frac{ku/a}{w - k(u + v_g)}\right)\times\left(\kappa_2(-a) - \kappa_2'(-a) + \frac{ku/a}{\omega + k(u - v_g)}\right) - \left(\kappa_1'(a) - \kappa_2(a) - \frac{ku/a}{\omega - ku - ku_g}\right)\times\left(\kappa_1(-a) - \kappa_2'(-a) + \frac{ku/a}{\omega + ku - kv_g}\right)\times e^{-\psi_1 + \psi_2} = 0, \tag{23}$$

where

$$\kappa_1'(a) = \kappa_1(a)\big|_{1/L_n = 0} \quad \text{and} \quad \kappa_2'(-a) = \kappa_2(-a)\big|_{1/L_n = 0}.$$

This dispersion relation includes both the K–H instability and the interchange or the resistive pressure-gradient-driven instability.

1. Case 2(a). Magnetic shear stabilization of K–H instability

The density gradient $1/L_n$ and v_g are set to zero in Eq. (23) to obtain

$$\frac{(ku/a)^2}{\omega^2 - k^2u^2}\exp\left(-2\int_{-a}^{a}q_r\,dx\right) + \left(2q_+ + \frac{ku/a}{\omega - ku}\right)\left(2q_- - \frac{ku/a}{\omega + ku}\right) = 0, \tag{24}$$

where q_r and q_i are a real and imaginary part of q, respectively, and $q_\pm = q(\pm a)$. As for the growing mode, we assume $\omega = i\gamma$ is pure imaginary. This assumption is justified since the imaginary part of the left-hand side of Eq. (24) is proportional to the real part of ω, which can be set to zero. Equation (24) is rewritten by keeping in mind $q_+ = q_-^* \equiv q_r(a) + iq_i(a)$ as follows:

$$\gamma^2 - \frac{kuq_i(a)}{a|q_+|^2}\gamma + \frac{1}{4|q_+|^2}\left(\frac{ku}{a}\right)^2\left[1 - 4aq_r(a) - \exp\left(-2\int_{-a}^{a}q_r\,dx\right) + 4a^2(q_r^2 + q_i^2)\right] = 0, \tag{25}$$

which yields

$$\gamma\left|\frac{a}{u}\right| = \frac{kq_i(a)}{|q_+|^2} \pm \frac{k}{2}\frac{2}{|q_+|^2}\left\{q_i^2(a) + |q_+|^2 \times\left[\exp\left(-2\int_{-a}^{a}q_r\,dx\right) - 4a^2|q_+|^2 + 4q_ra - 1\right]\right\}^{1/2}, \tag{26}$$

where

$$q_r(a) = [(s^2 + t^2)^{1/2} + s]^{1/2}/\sqrt{2}, \tag{27}$$
$$q_i(a) = -[(s^2 + t^2)^{1/2} - s]^{1/2}/\sqrt{2}, \tag{28}$$

and

$$s = k^2 + \frac{\nu(\nu + \gamma)/\rho_s^2}{(\nu + \gamma)^2 + k^2u^2} \simeq k^2 + \frac{\nu^2/\rho_s^2}{\nu^2 + k^2u^2}, \tag{29}$$
$$t = \frac{\nu ku/\rho_s^2}{(\nu + \gamma)^2 + k^2u^2} \simeq \frac{\nu ku/\rho_s^2}{\nu^2 + k^2u^2}. \tag{30}$$

Since $q_i(a)$ in Eq. (26) is negative, the K–H mode is unstable when

$$\exp\left(-2\int_{-a}^{a}q_r\,dx\right) - [2q_r(a)a - 1]^2 - 4q_i^2(a)a^2 > 0. \tag{31}$$

Roughly speaking, the maximum growth rate is at $q_r(a)a \simeq ka \simeq \frac{1}{2}$ and the threshold with respect to the parallel wave number is

$$ak_\parallel(a) < 0.30\sqrt{u\rho_s^2/v_e l_e a}. \tag{32}$$

When the shear scale length L_s is shorter than

$$L_s = 1.65(v_e l_e a/u\rho_s^2)^{1/2}, \tag{33}$$

all of the K–H mode will be stabilized.

2. Case 2(b)

Without shear flow and magnetic shear, the dispersion relation (24) gives the growth rate of the interchange instability for a finite density gradient. Equation (23) reduces to

$$\tanh(2aq) = -2kq/(k^2 + q^2), \tag{34}$$

where we assume $kL_n \simeq L_n/\rho_s \gg 1$ and approximate

$$\kappa_{1,2} \equiv \pm q,$$
$$q = k\left[1 + (g/L_n/(\omega - kv_g)\omega)\right]^{1/2}. \tag{35}$$

Setting $q = iz$, Eq. (34) becomes

$$f(z) = \tan(2az) = 2kz/(z^2 - k^2). \tag{36}$$

Solutions of the dispersion relation correspond to the cross points of Fig. 2. As seen in Fig. 2, the solutions of $|z/k| < 1$ are approximately given by

$$za \simeq (\pi/2)l, \quad l = \pm 1, \pm 2, \ldots, \tag{37}$$

which yields the frequency

$$\omega = \frac{kv_g}{2} \pm \frac{i}{2}\sqrt{\frac{k^2g/L_n}{k^2 + \pi^2l^2/4a^2} - k^2v_g^2}. \tag{38}$$

Therefore the mode is unstable when

$$a^2\omega_{ci}^2/gL_n > k^2a^2 + (\pi l/2)^2.$$

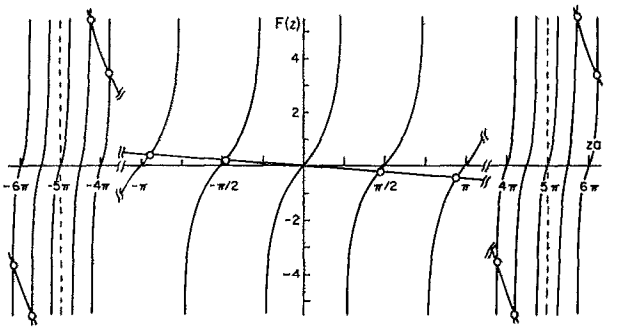

FIG. 2. Graphical location of roots of the eigenvalue problem given by intersection of $F(z) = \tan(2az)$ and the right side of Eq. (37).

Since $g \simeq c_s^2/R$ for the magnetic field curvature R and $R \gtrsim L_n$, the mode is unstable up to $k \gtrsim 1/\rho_s$.

3. Case 2(c)

Finally, we briefly discuss the velocity shear effects on the interchange instability in a finite density gradient. By a process similar to the derivation of Eq. (36) from Eq. (23), we rewrite Eq. (23) without any approximation to obtain

$$\tan\left(-i\int_{-a}^{a} q(x)dx\right) = \frac{iT}{S}, \tag{39}$$

where

$$S = q_+ q_- + \left(\kappa_- - \frac{1}{2L_n}\right)\left(\kappa_+ + \frac{1}{2L_n}\right) - \frac{ku}{a}\frac{\kappa_+ + 1/2L_n}{\omega - kv_g + ku} + \frac{ku}{a}\frac{\kappa_- - 1/2L_n}{\omega - kv_g - ku} - \frac{k^2u^2/a^2}{(\omega - kv_g)^2 - k^2u^2}, \tag{40}$$

$$T = \left(-\frac{1}{2L_n} + \kappa_-\right)q_+ + \left(\kappa_+ + \frac{1}{2L_n}\right)q_- - \frac{ku}{a}\frac{q_+}{\omega - kv_g + ku} + \frac{ku}{a}\frac{q_-}{\omega - kv_g - ku}, \tag{41}$$

$$\kappa_\pm = [k^2 + iv/\rho_s^2(\omega \mp ku - iv)]^{1/2}. \tag{42}$$

Here we used relations

$$\kappa_{1,2} = +1/2L_n \pm q_\pm \tag{43}$$

and

$$q_\pm = q(\pm a). \tag{44}$$

Since the dispersion relation of Eq. (39) is similar to Eq. (36), the solution of Eq. (39) is approximately given by

$$\int_{-a}^{a} q(x)dx = i\frac{\pi}{2}l + \delta \quad (l = 0, \pm 1, \pm 2, \ldots), \tag{45}$$

which corresponds to Eq. (37), where δ is a phase factor of the order unity. The WKB approximation that was used to derive Eq. (19) is valid when the integer l is sufficiently large. Assuming $kL_n \gg 1$, $q(x)$ is approximated by

$$q(x) = \left(k^2 - \frac{(kv_g - iv)kc_s/L_n\rho_s}{(\omega - kv_0)(\omega - kv_{E0} + iv)} + \frac{iv/\rho_s^2}{\omega - kv_{E0} + iv}\right)^{1/2}. \tag{46}$$

There are two resonances in Eq. (44), which are located at

$$x_{r1} = [(\omega - kv_g)/ku]a$$

and

$$x_{r2} = [(\omega + iv)/ku]a.$$

When $|v| \ll kv_g$, i.e., the magnetic shear is small enough, the distance between the two resonance points is $av_g/|u|$. Evaluating $q(x)$ at the center of the two resonances, namely,

$$q\left(-\frac{v_g a}{2u}\right) \simeq k\left(1 - \frac{4g}{L_n}\frac{1}{k^2v_g^2 - 4\omega^2}\right)^{1/2},$$

the growth rate obtained from Eq. (46) is roughly evaluated to be

$$\mathrm{Im}\,\omega = \frac{|k|v_g}{2}\sqrt{\frac{4ga^2/L_nu^2}{(\pi^2/4)l^2 + k^2a^2v_g^2/u^2} - 1}. \tag{47}$$

Therefore if

$$\frac{1}{\sqrt{\mathscr{R}}} \equiv \sqrt{\frac{g}{L_n}}\frac{a}{u} < \frac{\pi}{4}l, \tag{48}$$

the interchange mode is stabilized by the shear flow. Note that $\mathscr{R} = |L_n/g|(u/a)^2$ is the Richardson number. According to Chandrasekhar's textbook,[22] $\mathscr{R} < 1$ is given as the stabilization condition of K–H instability as for the gravity in the stable direction.

In unmagnetized plasmas the linearized equation, including equilibrium shear flow and gravity, is derived from the inviscid and incompressible fluid equations. The similar equation has been derived by Chandrasekhar,[22] in which the effect of gravity on the K–H instability is discussed. The result is

$$\frac{1}{\rho_0}\frac{d}{dx}\left(\rho_0\frac{dv_x}{dx}\right) = \left(k^2 + g\frac{k^2\rho_0'/\rho_0}{(\omega - kv_0)^2} + \frac{kv_0''}{\omega - kv_0} + \frac{kv_0'\rho_0'/\rho_0}{\omega - kv_0}\right)v_x. \tag{49}$$

As for the shear flow stabilization of the Rayleigh–Taylor instability, the stabilization condition for the configuration of case 1 is exactly the same as that given by Eq. (18). The criterion of Eq. (48) for case 2 is also applicable to Eq. (49).

III. INITIAL VALUE SIMULATION OF SHEAR FLOW INSTABILITIES

The static uniform magnetic field B_0 is now in the z direction only. The initial ion density is uniform, $n_i = n_0$, in the x-y plane. The plasma is encased in a metallic box in the x direction with $\phi(x = \pm L_x/2) = 0$ and periodic in the y direction for most of the computer experiments we present, unless otherwise specified. The particle velocities are reflected at the x boundaries. We load the electrons with a density given by

$$n_e(x,t=0) = n_0 + \Delta n_0/\cosh^2(k_0 x), \tag{50}$$

where typically $\Delta n_0 = 0.1 n_0$ and $k_0 = 1/a$, with a being the shear layer width of the $E \times B$ flow produced by the charge separation $\rho_q = e[n_e(\infty) - n_0]$. The initial flow of the plasma produced by the charge or vorticity layer given in Eq. (50) is

$$v_y(x) = (4\pi n_0 ec/k_0 B_0)(\Delta n_0/n_0)\tanh(k_0 x)$$
$$\equiv v_0 \tanh(x/a). \tag{51}$$

Although we vary parameters over a wide range, the typical set of parameters are as follows: the numbers of the grid points in the x and y directions $L_x = L_y = 64$, the numbers of particles in the x and y directions $N_x = N_y = 192$, the electron cyclotron frequency $\omega_{ce} = 80\omega_{pe}$ with ω_{pe} being the electron plasma frequency, the ion-to-electron mass ratio $M/m = 1600$, the shear width $a = k_0^{-1} = 6\Delta$ with Δ being the unit grid separation, the electron and ion Debye lengths perpendicular to the external magnetic field direction $\lambda_{De} = \lambda_{Di} = 0$, the electron and ion Larmor radii $\rho_e = \rho_i = 0$, and the simulation time step $\Delta t = 200\omega_{pe}^{-1}$. (In other words, particles are loaded cold with no thermal velocities in the directions perpendicular to the B field. No temperature development is seen well beyond the linear stage. The shear width is input as $a = 5\Delta$, which gives rise to the effective shear width of 6 as a result of the finite size particle effect.) Note that $(\omega_{pi}/\omega_{ci})^2 = (m_i/m_e)(\omega_{pe}/\omega_{ce})^2 = \frac{1}{4}$, which is orders of magnitude smaller than that of the usual fusion plasmas. Instead of assigning a uniform weight of unity to an individual particle, the weight of the particle is determined by the fraction $n_e(x)/n_0$ dependent upon its initial location. The weight of the particle in the simulation is not changed throughout the run. In the reference simulations we choose $\Delta n_0/n_0 = 0.1$, the size of particles $a_x = a_y = 3\Delta$, and the decentering parameter[16] $\gamma_i = \gamma_e = 0.1$.

The linear theory[1,5,23] for the hyperbolic tangent profile of Eq. (51) gives that the Kelvin–Helmholtz mode is unstable for the wave numbers k_y, satisfying

$$k_y a < 1, \tag{52}$$

where $k_y = 2\pi m/L_y$ and m is the mode number in the y direction. Figure 3 shows the electric potential $|\Phi|^2$ as a function of time for each mode ($m = 1$–4). Notice that because of the lack of noise in the implicit particle code, a large number of decades of exponential growth of the instability is observable. After a short period of time modes with $m = 1$ and 2 grow exponentially in time, while modes $m = 3$ and 4 do not grow until well into the nonlinear stage $t \sim 5\times 10^4 \omega_{pe}^{-1} = 31a/v_0$. Here recall that the threshold mode number $m_c = L_y/a = \frac{64}{5}$ and $m = 1,2$ are supposed to be linearly unstable and $m \geqslant 3$ are stable. This is in agreement with simulation in Fig. 3. For these simulation parameters $\tilde{v} \equiv v_y(x = L_x)\Delta t/\Delta$ is equal to 0.75. The $m = 2$ mode shows a slight oscillatory feature, as seen near $t = 8\times 10^4 \omega_{pe}^{-1} = 50a/v_0$. The modes with larger mode numbers are triggered unstable after the amplitude of the linearly unstable modes becomes high enough and the vortices of these modes begin to interfere or overlap around $t \sim 5\times 10^4 \omega_{pe}^{-1}$.

Figure 4 exhibits a typical particle plot and the corresponding electrostatic potential contours. For clarity, only particles with initial velocity $v_y > 0$ on the left half at $t = 0$ are shown. Figure 4 is at $t = 1\times 10^5 \omega_{pe}^{-1} = 62.5a/v_0$. In Fig. 5 we show the measured and theoretical growth rates of the modes. Figure 5 also shows the measured growth rate for the case when the magnetic field B_0 is tilted toward the y direction from the z direction by angle $\theta = 0.010$ rad. Note that this is less than the critical angle $(m_e/M_i)^{1/2} = 0.025$ rad. In this case the flow is still unstable although the magnitude of the growth rate is reduced by a factor of one order of magnitude and the unstable wave number increases, as is characteristic of drift-wave-like modes. On the other hand, when we tilt the magnetic field away from the z axis by $\theta = 3\times 10^{-2}$, the system is stable. The electron thermal speed v_{th} is taken to be $0.05\omega_{pe}\Delta$ in the tilted **B** field runs where electrons can move along the magnetic field line, while the thermal velocity perpendicular to **B** remains zero. Thus $k_\parallel v_{th} = 9.8\times 10^{-4} m\omega_{pe}$ for the $\theta = 10^{-2}$ case, where m is the mode number in the y direction. Thus $\gamma_{max} < k_\parallel v_{th}$, where $\gamma_{max} = 1.25\times 10^{-4}\omega_{pe} = 0.20 v_0/a$ for the K–H mode (in Fig. 5). For $\theta = 3\times 10^{-2}$, $k_\parallel v_{th} \gg \gamma^{K\text{-}H}$. The measured maximum growth rate for $\theta = 10^{-2}$ is $0.26\times 10^{-4}\omega_{pe}$, about one-fifth of the $\theta = 0$ case. When the normal mode is marginally stable, we find that the growth of

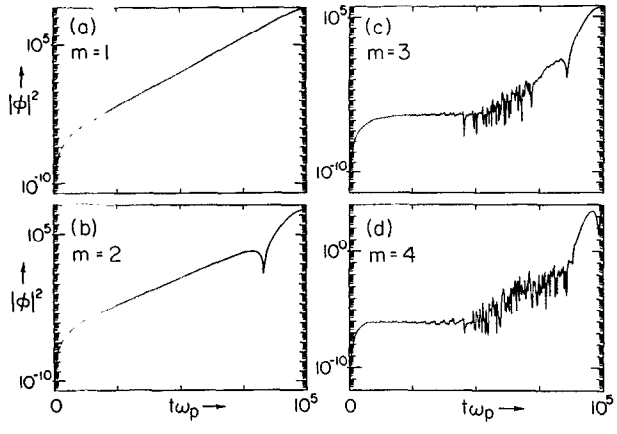

FIG. 3. Evolution of the electric potential $\Phi_m^2(t)$ for modes $m = 1,2,3,4$ for the reference parameters in Sec. III.

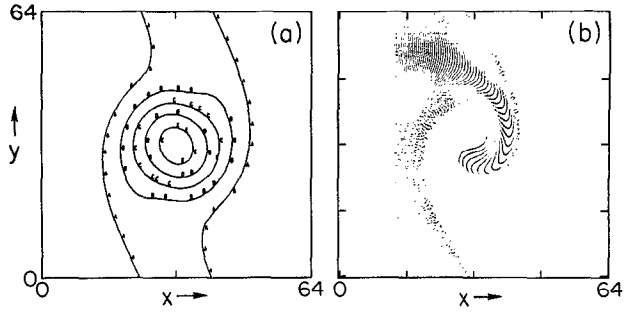

FIG. 4. (a) Contour plot of the electrostatic potential at the critical time shown in (b). (b) Position of particles in the (x-y) plane with initial fluid velocities $v_y < 0$ at a critical stage of dynamics just before wave breaking.

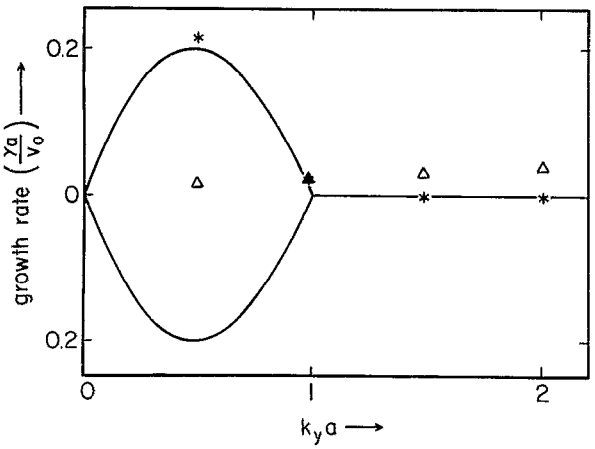

FIG. 5. Comparison of the measured growth rates with theoretical growth rate for the collisionless piecewise linear slab flow. For the * data the tilt angle θ of the magnetic field is zero and for the Δ data the tilt angle is $\theta = 0.010$/rad.

the mode becomes secular, as seen in Fig. 6. The electric potential resulting from the marginally unstable mode increase linearly with time.

As has been shown in the earlier driven simulations,[5] the stage at which the nonlinear triggering of other mode numbers sets in is coincident with the development of a vortex chain. In order to better control the study of the nonlinear problem of vortex evolution, our approach here is to separate the linear and nonlinear stages. We idealize the problem by starting from the secondary equilibrium of a vortex chain.

IV. NONLINEAR EVOLUTION OF VORTICES

A. Comparison with implicit particle simulation

In this section we initialize the simulation near the Stuart–Kelvin cat's eye equilibrium.[24,25] In the plasma context this amounts to the following initial electron density:

$$n_e(x,y) = n_0 + \frac{\Delta n_0(1-\epsilon^2)}{[\cosh(k_0x) + \epsilon\cos(k_0y)]^2}, \tag{53}$$

where $0 \leqslant \epsilon < 1$. The ion density is taken to be uniform $n_i = n_0$. The electrostatic potential resulting from these charge densities is

$$\phi(x,y) = (v_0/k_0)\ln[\cosh(k_0x) + \epsilon\cos(k_0y)]. \tag{54}$$

Thus the secondary equilibrium flow is given by

$$v_x = \epsilon v_0 \sin(k_0y)/[\cosh(k_0x) + \epsilon\cos(k_0y)],$$

$$v_y = \frac{v_0\sinh(k_0x)}{\cosh(k_0x) + \epsilon\cos(ky_0)}.$$

For $\epsilon = 0$, Eq. (53) reduces to Eq. (50). As ϵ is increased, the island structure of the equidensity contours becomes wider in the x direction. We load electrons of nonuniform weight to describe the nonuniform density distribution, and the parameters are the same as in Sec. III. With these parameters fixed, we vary ϵ from zero to the following set of values: 0.08, 0.3, 0.5, 0.6, 0.7, 0.85, and 0.95. The unit of frequency ω_{pe} is measured where $n_e = n_0$, $L_n/a = 64.5$, and the hydrodynamic unit of time a/v_0 at $x = 0$ or L_x is given by $a/v_0 \sim 1.6\times 10^3\omega_{pe}^{-1}$.

Figure 7 shows snapshots of particles with (x,y) coordinates and the corresponding electric potentials at various times for the case of $\epsilon = 0.08$. The instability is triggered by

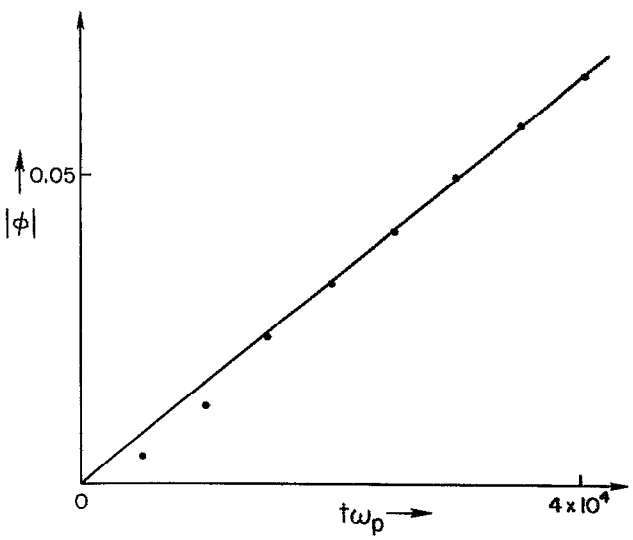

FIG. 6. Secular growth of the potential with a linear increase in time for a marginally stable mode.

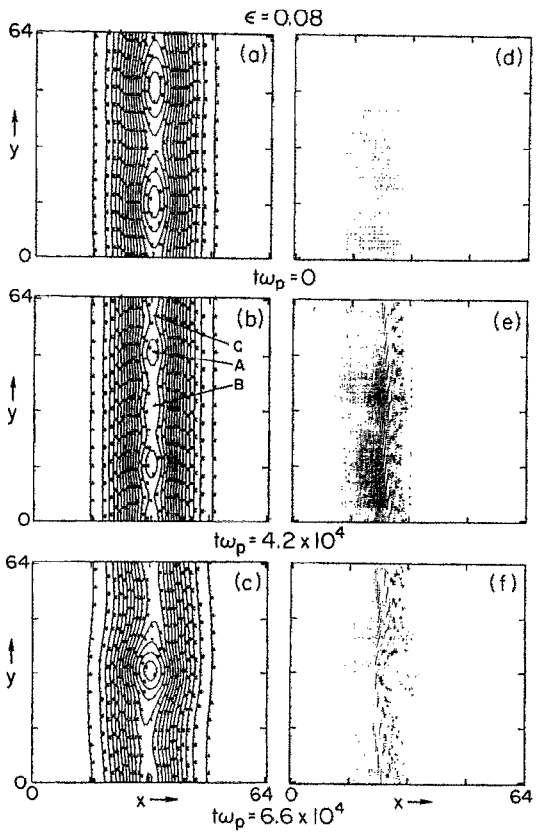

FIG. 7. (a)–(c) Contours of the electrostatic potential for the period-doubling coalescence from the $m = 2$, $\epsilon = 0.08$ island chain. (d)–(f) Particles starting with $v_y < 0$ at later stages of the coalescence instability evolving from the period island chain of strength $\epsilon = 0.08$.

noise due to numerical truncation that results upon loading the particles, as there is no noise associated with the particle motion perpendicular to B with the initialization and the subsequent decentering algorithm.[16] At $t = 4.2\times 10^4 \omega_{pe}^{-1} = 26a/v_0$ the contour lines show a reconnection of the flow lines, reminiscent of the tearing instability of magnetic islands, which yields vortices (islands) with smaller wavelengths ($m = 4$). Note the original vortices had mode number $m = 2$. At a later time the smaller induced islands ($m = 4$) are absorbed by the original islands ($m = 2$). At a later time the smaller induced islands ($m = 4$) are absorbed by the original islands ($m = 2$). In Figs. 7(c) and 7(f) at time $t = 6.6\times 10^4 \omega_{pe}^{-1} = 41a/v_0$, we observe that the larger original vortices coalesce into one vortex with $m = 1$ in the direction of the exterior flow. We also see the vortex tilts in the clockwise sense as a result of the ambient external flow, which is downward on the right side of the vortex and upward on the left side.

During the coalescence process the perturbed electrostatic potential energy grows exponentially in time as shown in Fig. 8(a). Figure 8 summarizes the growth of the electrostatic energy for cases with various values of ϵ. The saturation of this energy in Fig. 8(a) occurs shortly after a complete coalescence.

As we raise the value of ϵ, with other parameters being fixed as before, the growth rate of the electrostatic energy increases, as shown in Fig. 9. This figure will be further discussed in Sec. V. In frames (b)–(d) of Fig. 8 we also observe that a slight bump develops in the middle of the otherwise exponential growth phase. In particular, Fig. 8(d) shows a faster than exponential growth in the early stage, while settling into a nearly exponential growth later. This indicates a transient growth that is faster than exponential growth for $\epsilon > \epsilon_{crit} \approx 0.5$. Another feature to be noticed in Fig. 8 is the amplitude oscillations after the coalescence. These are associated with the ringing of the vortex shape. This is reminiscent of the coalescence process of magnetic islands, although any parallelism of the coalescence of vortices in the present investigation with that of the magnetic island coalescence is perhaps fortuitous since the dynamical equations are rather different. Some conspicuous differences in the governing

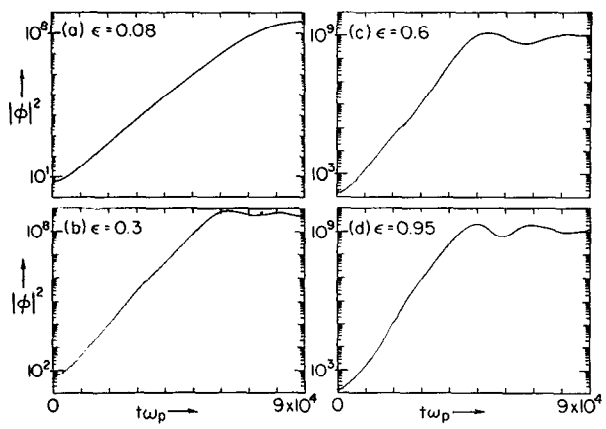

FIG. 8. Evolution of the electrostatic potential energy from the nonlinear island chain as a function of increasing vortex strength ϵ.

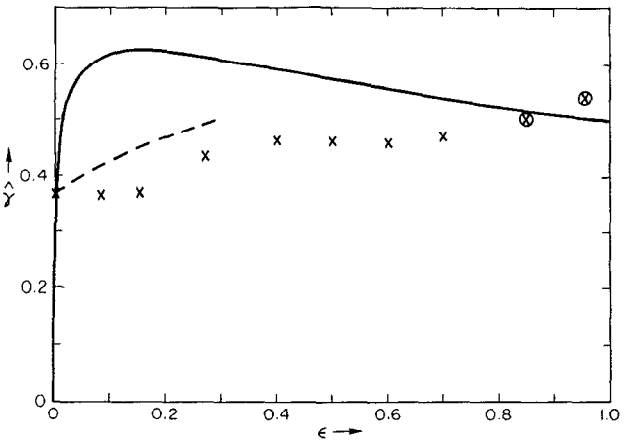

FIG. 9. Plot of normalized linear growth rate $\hat{\gamma}$ vs ϵ: $\times$ represents a data point extracted from the simulation results, $\otimes$ is a data point where it is difficult to ascertain the growth rate because the growth is faster than exponential. The dashed curve is the linear theory of Ref. 25; the solid curve is that derived from the localized vortex model.

physics include (i) the vortex dynamics is described by the single field ϕ, while the magnetic island dynamics requires at least two fields ϕ and the z component of vector potential A_z; (ii) consequently, there exists a magnetic repulsive force upon magnetic island coalescence, while in the vortex dynamics there is none; and (iii) the magnetic flux conservation inhibits the reconnection of the magnetic flow lines. On the other hand, the presence of the Kelvin–Helmholtz instability and the coalescence instability for the vortex dynamics is similar to the presence of the tearing instability and the magnetic coalescence instability, except for the frozen flux constraint that $d\psi/dt = \eta\nabla^2\psi \to 0$. The importance of the flux conservation constraint is easily seen in the formulas for the linear growth rates where $\gamma^{K\text{-}H} \sim k_y \Delta v_y$ but $\gamma^t \propto k_y^{2/3}\eta^{3/5}$.

In light of the above the actual dynamics of the tearing mode is, in principle, different from that for vortex coalescence dynamics. Ideas used to study the tearing, however, can be used to measure the vortex dynamics observed here. One measure is the vorticity difference between the original O point and the innermost X point (e.g., between A and B in Fig. 7 and Fig. 12), and another measure is the vorticity difference between the original O point and the outermost X point (e.g., between A and C in Fig. 7 and Fig. 12). The former measure of vorticity is indicated by circles and the latter measure by crosses in Fig. 10, for various ϵ cases. By definition of the former, the measure of vorticity vanishes when the two vortices complete their coalescence. Compare Fig. 10 with Fig. 8. On the other hand, the latter measure of vorticity may or may not vanish. In small ϵ runs [Figs. 10(a) and 10(b)], we see that it decreases until a certain point ($t \simeq 5\times 10^4 \omega_{pe}^{-1} = 38.6a/v_0$) and then begins to increase. This manifests itself in a larger vortex at $t = 6.6\times 10^4 \omega_{pe}^{-1} = 51a/v_0$ [e.g., Fig. 7(c)] than the original vortex. In larger ϵ experiments [Figs. 10(c) and 10(d)] the two measures depart, but both measures decrease, or at least not increase, even well after the coalescence.

Let us further examine the cases with $\epsilon = 0.3$ and

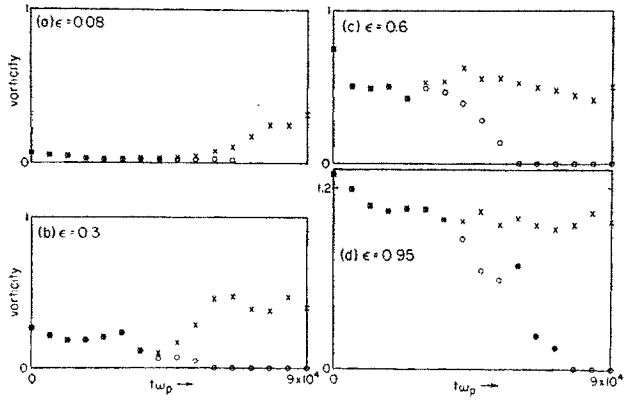

FIG. 10. A measure of the vorticity in the trapped coherent structures. The vorticity difference between the original O point to the innermost X point is given by the circles (○) and vorticity difference between the original O point and the outermost X point is given by the crosses (×).

$\epsilon = 0.6$, which are shown in Figs. 11 and 12, respectively. Figure 11(c) shows skewness of each vortex, as well as the tilt of the axis of the two vortex centers, measured in the negative direction. This is similar to the prediction by Liu *et al.*[1] and one found in the simulation.[5] A more pronounced tilt may be seen in Fig 12. The rotation of the axis continues even after the completion of the coalescence. Thus we find that the chain of vortices is unstable against the tilt or rotational instability. In Figs. 12(a)–12(d) we observe the rotation of the axis that connects the two O points as they approach each other. Even after the coalescence the rotation continues. At the same time the overshooting oscillation (squashing of the droplet) continues. In this particular case, where $\epsilon = 0.6$, during the course of these droplet vibrations, fission of the vortex occurs, as seen in Fig. 12(d). Observe in Fig. 12 that as the $m = 2$ vortices coalesce into an $m = 1$ vortex, much smaller-scale vortices spring up. As the energy inversely cascades from the $m = 2$ vortices to the $m = 1$ vortex, the enstrophy cascades from $m = 2$ to higher m's, since both the overall enstrophy and energy are conserved. From the distribution of particles in plots in Figs. 7, 11, and 12, we note that even when the potential contours show fairly coherent patterns, the particles are strongly mixing in complex structures.

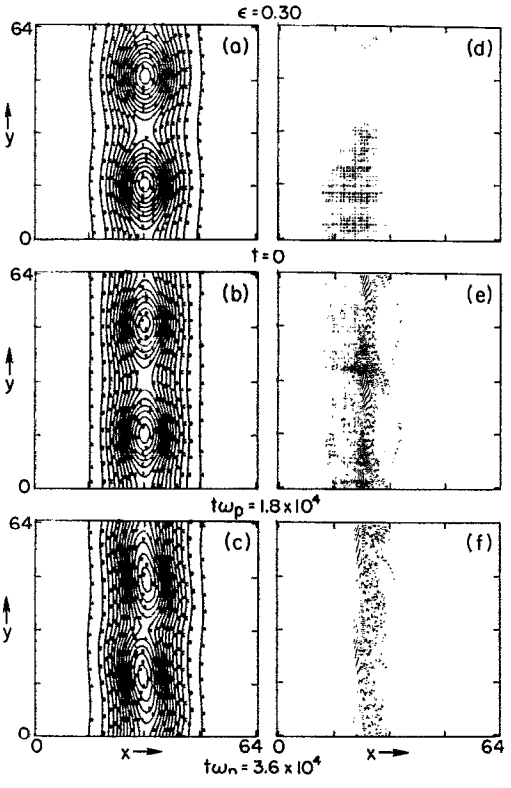

FIG. 11. Potential contours (a)–(c) and particle plots (d)–(f) for the period-doubling coalescence of the $m = 2$, $\epsilon = 0.30$ island chain. The skewness of each vortex as the axis between two vortex centers rotates during coalescence.

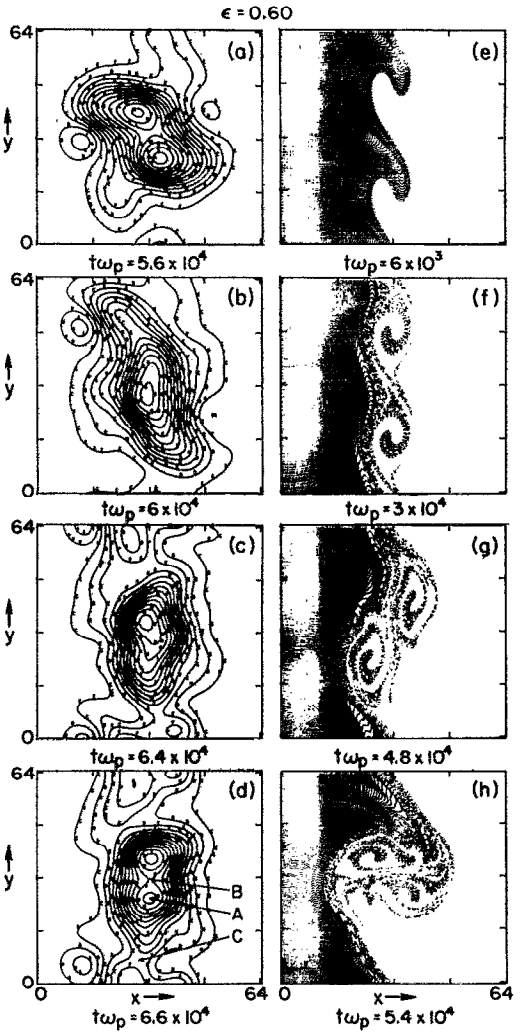

FIG. 12. As in Fig. 11, but a case of $\epsilon = 0.6$ with stronger tilting, where the rotation continues after coalescence.

In Fig. 13 the negative of the rotational angle of the vortex–vortex axis as a function of time is measured. As ϵ is increased, so is the growth of the angle. The rate of increase of the angle before $\theta = 180°$ is found to be faster than expo-

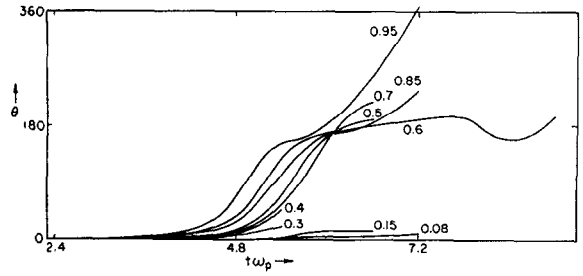

FIG. 13. Simulation measurements for the rotation angle as a function of time $\theta(t)$ for labeled values of ϵ.

nential. Following the terminology of magnetic coalescence this growth is called explosive growth. This explosive increase of θ saturates at or near $\theta = 180°$. In some cases θ stays around 180° after it reaches this position. In other cases, after a brief pause at $\theta = 180°$ the angle again increases. The higher value of θ, the stronger is this tendency for continued rotation. Figure 14 displays the distance between the two O points as a function of time. Once again this distance $\delta r(t) = \sqrt{\Delta x^2 + \Delta y^2}$ also grows faster than exponential during the coalescence, indicating the explosive nature of the transients in the coalescence process. Note that different from θ in Fig. 13, the dependence of δr as a function of ϵ is not monotonically increasing. Also noted is that the increase of δr as a function of time is sometimes not monotonic.

Figure 15 shows the potential ϕ at $t = 0$ and a later time at which point a nearly $\pi/2$ rotation of the axis of a pair of vortices is realized for the $\epsilon = 0.3$ and $\epsilon = 0.7$ cases. The evolution will be later compared with the theoretical model in Sec. IV B.

B. Localized vortex model

We now present techniques for analytically modeling vortex simulation results, such as those presented in Secs. III and IV A, by simple few degree-of-freedom Hamiltonian

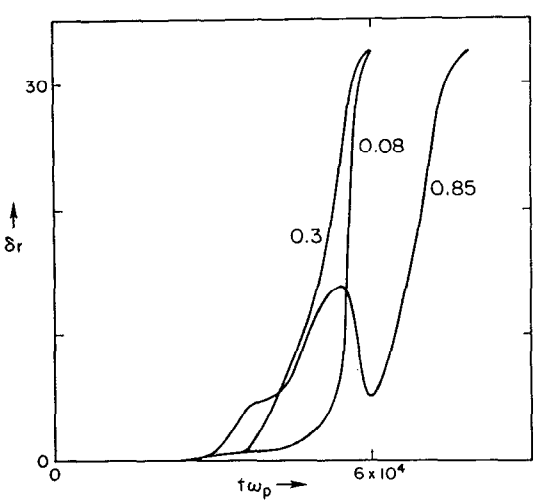

FIG. 14. The distance between two O points as a function of time $\delta r(t)$, as measured in the simulation for the labeled values of ϵ.

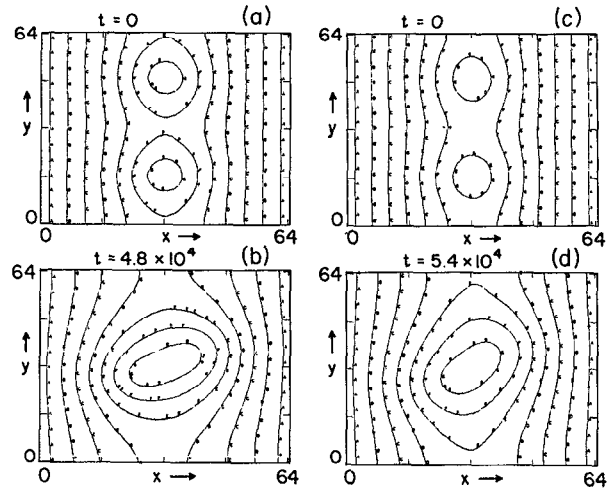

FIG. 15. Equipotential contours obtained from the simulation: (a) $\epsilon = 0.95$, $t = 0$; (b) $\epsilon = 0.95$ at a later time; (c) $\epsilon = 0.7$, $t = 0$; (d) $\epsilon = 0.7$ at a later time.

systems. This is a plausible goal, as the system is nearly dissipationless and low wave number modes dominate the dynamics. The specific application of these techniques to the near cat's eye simulations are considered. The goal here being to elucidate the dynamical mechanisms that are active during the coalescence or tilt instabilities.

The simulation results suggest that there is a large temporal regime where the two localized vortices of the initial condition remain isolated and maintain their integrity while moving. This suggests a few degree-of-freedom models for the flow, composed of localized interacting vortices, perhaps subject to an external field.

Since the computational studies of this paper are periodic in the y direction, but not the x direction, these boundary conditions must be incorporated into a model of the dynamics. The x boundary condition is straightforward, since to a large degree the motion of the localized vortices is far enough removed from the boundaries for us to assume $-\infty < x < \infty$. More generally, one can satisfy finite metallic boundary conditions by appropriate configurations of image vortices. This is not pursued here for the x direction, but the periodic y boundary condition does require images. These boundary conditions are perhaps a bit confusing since the simulations have a periodicity length of $4\pi/k_0$, while the initial conditions of interest are nearly $2\pi/k_0$ periodic. This latter condition near periodicity is not a constraint of the dynamics; thus unlike the $4\pi/k_0$ periodicity should not be built into the vortex model.

Begin by supposing that there are two vortices in the simulation domain: one denoted by "0" and the other by "1." Periodicity in the y direction requires that each of these vortices be tracked by an infinite chain of equal strength image vorticities. Vortices that track vortex 0 will be denoted by an even subscript, while those that track vortex 1 will be denoted by an odd subscript. The periodicity requirement thus demands the following constraints:

$$
\begin{aligned}
y_{2n}(t) &= y_0(t) + 4\pi n/k_0, \\
y_{2n+1}(t) &= y_1(t) + 4\pi n/k_0, \\
x_{2n}(t) &= x_0(t), \\
x_{2n+1}(t) &= x_1(t),
\end{aligned} \tag{55}
$$

where $n = \pm 1, \pm 2, \pm 3, \ldots$.

In general, suppose that the velocity at vortex n located at $\mathbf{x}_n \equiv (x_n, y_n)$, resulting from vortex m located at x_m, is given by

$$
\mathbf{v}_{nm} = \mathbf{V}(\mathbf{x}_n - \mathbf{x}_m). \tag{56}
$$

Upon superposing, the total velocity at the location of vortex 0 is given by

$$
\mathbf{v}_0 = \sum_{\substack{m=-\infty \\ m\neq 0}}^{\infty} \mathbf{V}(\mathbf{x}_0 - \mathbf{x}_m). \tag{57}
$$

Similarly, for vortex 1,

$$
\mathbf{v}_1 = \sum_{\substack{m=-\infty \\ m\neq 1}}^{\infty} \mathbf{V}(\mathbf{x}_1 - \mathbf{x}_m). \tag{58}
$$

Suppose that $\mathbf{V}$ is derivable from a streamfunction, defined by

$$
\mathbf{V}(x,y) = \hat{z} \times \nabla \psi(x,y), \tag{59}
$$

where ψ is even in both of its arguments,

$$
\psi(x,y) = \psi(-x,y) = \psi(x,-y). \tag{60}
$$

Making use of these symmetry conditions and the periodicity constraints of Eq. (55) yields the following for Eqs. (57) and (58):

$$
\begin{aligned}
\mathbf{v}_0 &= \sum_{m=-\infty}^{\infty} \hat{z} \times \nabla \psi\left(x_0 - x_1, y_0 - y_1 - \frac{4\pi m}{k_0}\right), \\
\mathbf{v}_1 &= \sum_{m=-\infty}^{\infty} \hat{z} \times \nabla \psi\left(x_1 - x_0, y_1 - y_0 - \frac{4\pi m}{k_0}\right).
\end{aligned} \tag{61}
$$

We ignore the self-interaction of the vortices and assume they move with the local flow. This yields the following Hamiltonian equations of motion:

$$
\dot{x}_i = -\frac{\partial H}{\partial y_i}, \quad \dot{y}_i = \frac{\partial H}{\partial x_i}, \quad i = 0,1, \tag{62}
$$

where

$$
H(x_0 - x_1, y_0 - y_1) \equiv \sum_{m=-\infty}^{\infty} \psi\left(x_0 - x_1, y_0 - y_1 - \frac{4\pi m}{k_0}\right). \tag{63}
$$

The form of the Hamiltonian of Eq. (63) suggests the introduction of the "center-of-mass" coordinates, defined by

$$
\begin{aligned}
\xi &= x_0 - x_1, \quad \eta = y_0 - y_1, \\
\mathscr{X} &= x_1 + x_0, \quad \mathscr{Y} = y_1 + y_0.
\end{aligned} \tag{64}
$$

The coordinates $(\mathscr{X}, \mathscr{Y})$ remain fixed in time while (ξ,η) satisfy

$$
\dot{\xi} = -\frac{\partial H}{\partial \eta}(\xi,\eta), \quad \dot{\eta} = \frac{\partial H}{\partial \xi}(\xi,\eta). \tag{65}
$$

In order to effect the modeling, the function $H(\xi,\eta)$ remains to be determined. This can be achieved in two ways: first, a model H can be obtained directly by tracking the relative motion of the vortices. Since for this system physical space (ξ,η) is the phase space, and since trajectories lie on curves of constant H, one can attempt to fit H to the simulation output. Alternatively the vortex–vortex interaction ψ can be postulated, perhaps, by examination of the vortex shape. Knowing ψ, the sum of Eq. (63) must be evaluated in order to determine the dynamics.

Sometimes the sum of Eq. (63) can be evaluated in closed form; for example, in the case of point vortices where

$$
\psi(\xi,\eta) = \psi_0 \ln(\xi^2 + \eta^2), \tag{66}
$$

this is the case. Defining $z = (k_0/4)(\eta + i\xi)$, it is evident that

$$
J = \frac{\partial H}{\partial \eta} - i\frac{\partial H}{\partial \xi} = \frac{k_0\psi_0}{2} \sum_{m=-\infty}^{\infty} \frac{1}{z - m\pi}. \tag{67}
$$

The sum of Eq. (67) is the Mittag–Leffler expansion for cot z, which implies

$$
J = \frac{k_0\psi_0}{2}\left(\frac{\sin(k_0\eta/2) - i\sinh(k_0\xi/2)}{\cosh(k_0\xi/2) - \cos(k_0\eta/2)}\right), \tag{68}
$$

and thus from the first equality of (67) we obtain, to within an additive constant,

$$
H(\xi,\eta) = \psi_0 \ln[\cosh(k_0\xi/2) - \cos(k_0\eta/2)]. \tag{69}
$$

The summation performed above is related to the solved classical problem of obtaining the velocity field as a result of an infinite chain of point vortices,[26] but here the context is different, in that H determines the dynamics subject to the constraints (55). Here H is not the streamfunction. Below we will construct the streamfunction as a function of time.

We propose the following form for H in the case where ε can differ from unity:

$$
H(\xi,\eta;\varepsilon) = \psi_0 \ln\left[\sqrt{\tfrac{1}{2}(\epsilon + \cosh k_0\xi)} - \sqrt{\epsilon}\cos(k_0\eta/2)\right]. \tag{70}
$$

Arguments in favor of this seemingly obscure choice will shortly be given, but first consider the inverse problem for obtaining $\psi(\xi,\eta;\varepsilon)$. Suppose ψ has the form of the point vortex interaction, except isotropy is broken by warping the x dependence of the interaction, i.e.,

$$
\psi(\xi,\eta;\epsilon) = \psi_0 \ln[f^2(\xi) + \eta^2], \tag{71}
$$

where the function $f(\xi)$ is yet to be determined. Substitution of f for ξ in our treatment of the point vortex case yields

$$
\frac{\partial H}{\partial \eta} = \frac{k_0\psi_0}{2} \frac{\sin(k_0\eta/2)}{\cosh(k_0 f/2) - \cos(k_0\eta/2)}, \tag{72}
$$

$$
\frac{\partial H}{\partial f} = \frac{k_0\psi_0}{2} \frac{\sinh(k_0 f/2)}{\cosh(k_0 f/2) - \cos(k_0\eta/2)}. \tag{73}
$$

Equations (72) and (73) imply

$$
H(\xi,\eta;\epsilon) = \psi_0 \ln[\cosh(k_0 f/2) - \cos(k_0\eta/2)] + \text{const.} \tag{74}
$$

Choosing the function f as follows:

$$
\cosh(k_0 f) = (1/\epsilon)\cosh(k_0\xi), \tag{75}
$$

results in, apart from an unimportant additive constant, the H given by Eq. (70).

There are several favorable attributes that lead one to choose the H of Eq. (70). To begin with, it is a continuous

deformation away from the case where $\epsilon = 1$, a case where the model agrees with the simulation [cf. Eq. (69)]. Thus at least near $\epsilon = 1$ we expect reasonable agreement. Inspection of Eq. (75) reveals that for $\epsilon \neq 1$ the logarithmic singularity at $\xi = \eta = 0$ has been eliminated. Any distributed vorticity arrangement will have this feature. Also, the anisotropy introduced is in agreement with that observed in the simulation (cf. Fig. 15). In particular, $\partial\psi/\partial\xi|_{\eta=0}$ dominates $\partial\psi/\partial\eta|_{\xi=0}$. A convincing argument in favor of the choice of Eq. (70) is that it leads to a $\phi(x,y,t)$, which, as we shall see, looks like the simulation. We emphasize, however, that this choice is not unique and only qualitative agreement is sought.

The construction of $\phi(x,y,t)$ requires that the contributions from the double infinity of vortices be summed at each moment of time. We conclude that

$$\phi(x,y,t) = \sum_{m=-\infty}^{\infty} \left[\psi\left(x - x_0, y - y_0 - \frac{4\pi m}{k_0}\right) + \psi\left(x - x_1, y - y_1 - \frac{4\pi m}{k_0}\right)\right]. \tag{76}$$

Without loss of generality the arbitrary constant can be dropped. Assuming

$$\begin{aligned} &\mathscr{X} = \mathscr{Y} = 0, \\ &x_0 = \tfrac{1}{2}\xi, \quad x_1 = -\tfrac{1}{2}\xi, \\ &y_0 = \tfrac{1}{2}\eta, \quad y_1 = -\tfrac{1}{2}\eta, \end{aligned} \tag{77}$$

yields

$$\phi(x,y,t;\epsilon) = H[x - \xi(t)/2, y - \eta(t)/2;\epsilon] + H[x + \xi(t)/2, y + \eta(t)/2;\epsilon]. \tag{78}$$

At time $t = 0$, Eq. (78) should represent the cat's eye initial condition. Using $\xi(t=0) = 0$, $\eta(t=0) = 2\pi/k_0$, Eq. (70) implies

$$\phi(x,y,0;\epsilon) = \psi_0 \ln[\cosh k_0 x + \epsilon \cos k_0 y], \tag{79}$$

the equilibrium state desired. At later times,

$$\begin{aligned} \phi(x,y,t;\epsilon) = \psi_0 \ln\Bigg(2\Bigg\{&\sqrt{\frac{1}{2}\left[\epsilon + \cosh k_0\left(x - \frac{\xi(t)}{2}\right)\right]} \\ &- \sqrt{\epsilon}\cos\frac{k_0}{2}\left(y - \frac{\eta(t)}{2}\right)\Bigg\} \\ &\times\Bigg\{\sqrt{\frac{1}{2}\left[\epsilon + \cosh k_0\left(x + \frac{\xi(t)}{2}\right)\right]} \\ &- \sqrt{\epsilon}\cos\frac{k_0}{2}\left(y + \frac{\eta(t)}{2}\right)\Bigg\}\Bigg). \end{aligned} \tag{80}$$

Now consider the comparison of the linear theory of the localized vortex model with the simulation. As noted above, $\xi = 0$ and $\eta = 2\pi/k_0$ correspond to the cat's eye equilibrium, but, also, these correspond to dynamical equilibrium of the localized vortex model. This is evident upon differentiating Eq. (70). Moreover, expanding H to second order yields the following Hamiltonian for the linearized dynamics:

$$h(\delta\xi,\delta\eta;\epsilon) = \frac{k_0^2\psi_0\sqrt{2}}{8[\sqrt{(1+\epsilon)} + \sqrt{2\epsilon}]}\left(-\sqrt{\epsilon}\delta\eta^2 + \frac{\sqrt{2}\delta\xi^2}{\sqrt{1+\epsilon}}\right). \tag{81}$$

Thus the linear growth rate based on this model, normalized by $k_0^2\psi_0/4$, is given by

$$\hat{\gamma} = 2^{3/4}\epsilon^{1/4}/(1+\epsilon)^{1/4}(\sqrt{1+\epsilon} + \sqrt{2\epsilon}). \tag{82}$$

For $\epsilon = 1$, $\hat{\gamma} = \frac{1}{2}$, the classical result for the maximum growth rate of a row of point vortices. The localized vortex model selects the maximum because this is the only motion allowed by the periodicity constraints of Eqs. (55). Examination of Fig. 16 reveals that the simulation is in agreement in this limit. As $\epsilon \to 0$, $\hat{\gamma} \sim 2^{3/4}\epsilon^{1/4}$. This vanishing growth rate is in disagreement with the simulation; not a surprising result since the assumption of localization of the vortices breaks down. Because of $\epsilon^{1/4}$ behavior this disagreement is confined to $0 \leqslant \epsilon \lesssim 0.2$. The theory is in reasonable agreement for a large range of ϵ away from unity. In Fig. 16 we have also plotted the results of Ref. 25, where the linear eigenvalue problem for the cat's eye equilibrium was solved numerically. Observe that for $\epsilon \sim 0.3$ there appears to be a transition from localized vortex behavior to what we refer to as K–H behavior, i.e., sustainment of $\hat{\gamma}$. This is further evidenced in Fig. 10. On the other hand, the theory[25] by Pierrehumbert and Windall is correct at $\epsilon = 0$ and agrees reasonably with simulation for $\epsilon < 0.3$, but is unable to converge beyond.

Now consider the nonlinear behavior. Since H is conserved, one can obtain the orbits in physical space by simply plotting surfaces of constant H. In Fig. 17 we have done so for different values of ϵ. This figure shows that the energy surface decreases in width as ϵ decreases from 1 to 0. In the simulation it was observed that for small values of ϵ the in-

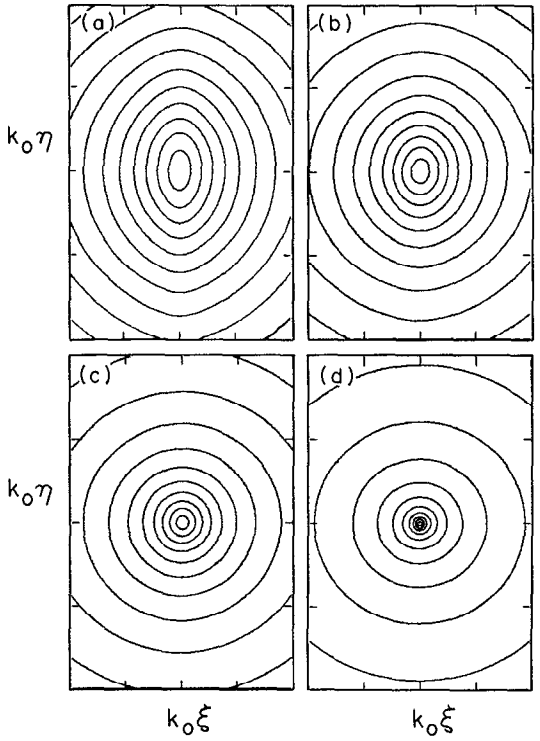

FIG. 16. Contours of the vortex–vortex interaction potential ψ given by Eqs. (75) and (79), for the cases (a) $\epsilon = 0.05$, (b) $\epsilon = 0.30$, (c) $\epsilon = 0.70$, and (d) $\epsilon = 1.0$.

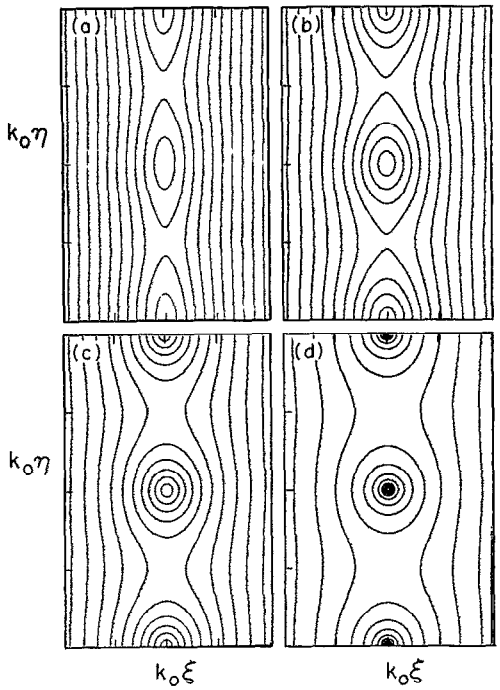

FIG. 17. Contours of constant interaction Hamiltonian, H, for (a) $\epsilon = 0.05$, (b) $\epsilon = 0.30$, (c) $\epsilon = 0.70$, and (d) $\epsilon = 1.0$.

stability that occurs is of the pairing or coalescence type, as shown in Fig. 10. For values of ϵ near unity the instability that occurs is of the tilt or rotational type. Figure 17 explains this tendency with ϵ. For all finite values of ϵ the vortices approach each other and move transverse to each other. For small ϵ the later motion decreases with the width of the energy surface and we observe the predominant coalescence.

In Fig. 18(b) we show the results of integrating Eqs. (65). Here $\theta(t)$ and $\delta r(t) = r(0) - r(t)$ for various values of ϵ are given. Many features of the corresponding quantities for the simulation Figs. 13 and 14 are reproduced, as seen in Fig. 18(a). The initial conditions here were chosen near the separatrix, either just inside or outside. In the case where the initial condition is just inside, θ can increase beyond 180°. This behavior is seen in Fig. 18(a) for the case where $\epsilon = 0.95$ and in Fig. 19(b) for the case with $\epsilon = 0.3$. When the initial condition is outside the separatrix, in the localized vortex model, θ can only approach 180°. This behavior is indicated in Fig. 18(a) by the flat spot near $\theta = 180°$ and shown in Fig. 18(b) for the case where $\epsilon = 0.3$. Similarly, Figs. 14 and 18 for $\delta r(t)$ show qualitative comparison.

Given the results of the orbit integration we can plot the streamfunction as a function of time by making use of Eq. (78). We have done so in Fig. 19(a) for the point vortex case where $\epsilon = 1$ and $t = 0$, while Fig. 19(b) shows ϕ for $\epsilon = 1$ and $t = \hat{t}$, a later time chosen so that $\theta \simeq \pi/2$. Similarly, in Figs. 19(c) and 19(d) we plot ϕ for the case where $\epsilon = 0.6$ and $t = 0$ and $t = \bar{t}$, respectively ($\bar{t}$ is chosen again so that $\theta \simeq \pi/2$). Figure 19 should be compared to Fig. 15.

In summary, we see that there is qualitative agreement between the simulation and the localized vortex model with increasingly better agreement for larger ϵ.

V. SUMMARY AND CONCLUSIONS

We have derived linear theoretical stability conditions and growth rates for a plasma with shear flows, taking into account gravity and magnetic shear. We analyzed the stability problem with a discontinuous background density and with a smoothly varying density. The dispersion relation shows the presence of $E \times B$ shear flows can stabilize the interchange and other related instabilities. The linear analysis of the gravitational instability shows that the interchange (R–T) mode is stabilized by the shear flow when the velocity shear $u/a \geq \sqrt{kg}$ or $\sqrt{g/L_n}$ [see Eqs. (18) and (48)]. In the case of the interchange mode, much shorter wavelength modes (much higher azimuthal modes) are destabilized. The mode is strongly localized near the mode rational surface. The interchange mode can be stabilized when $u/a \gtrsim (g/L_n)^{1/2}$.

Implicit particle simulation results of the shear flow (K–H) instability resulting from $E \times B$ drift in a magnetized plasma show good agreement with the linear theory. The maximum growth ($0.2u/a$) and the threshold wave number ($1/a$) agree well with the observed growth rate and threshold. The linear K–H instability with $k_{\parallel} = 0$ has a sharp boundary between the stable and unstable wave numbers, with the marginally stable modes having a local secular ($\sim t$) growth arising, perhaps, from a ballistic resonance. In contrast, three-dimensional (3-D) modes with $k_{\parallel}/k < \theta_c$ have a reduced growth rates. In the simulation, if the tilt angle $\theta \gtrsim 0.02$, the modes become drift-wave-like and the growth rate is greatly reduced, while the unstable wavelength band expands. In the K–H instability, vortices that grow to a sufficient size trigger a secondary nonlinear instability with smaller, subharmonic wave numbers.

The nonlinear instability is analyzed using a dynamic periodic chain of localized vortex structures with an equilibrium equivalent to the Kelvin–Stuart cat's eye type solution. This equilibrium is observed to be unstable against the coalescence and tilt modes. The electrostatic energy increase of a lower wave number mode ($m = 1$) (the growth rate of $m = 1$ mode) is in reasonable agreement with the theory by Pierrehumbert and Windall[25] and the analysis of Sec. IV B. In a small-amplitude regime, the tilt and coalescence instability and shear flow instability coexist. Even after the completion of coalescence, the shear flow instability continues. In the case of large amplitude, the tilt and coalescence instabilities dominate the shear flow instability. Upon overshoot of the tilt and coalescence, the coalesced vortices can again separate into two.

The growth rate of the tilt angle is in good agreement with the coalescence instability of a point vortex model in an appropriate range. The angle θ increases faster than the exponential function of time. The angle θ approaches π and stays for a long time. The point vortex model can accurately predict the time profile of the rotation angle of the vortices. The time scale prediction of the relative rotation of two vortices also provides a good explanation of the simulation.

The results for the stability of the transitional layer of a

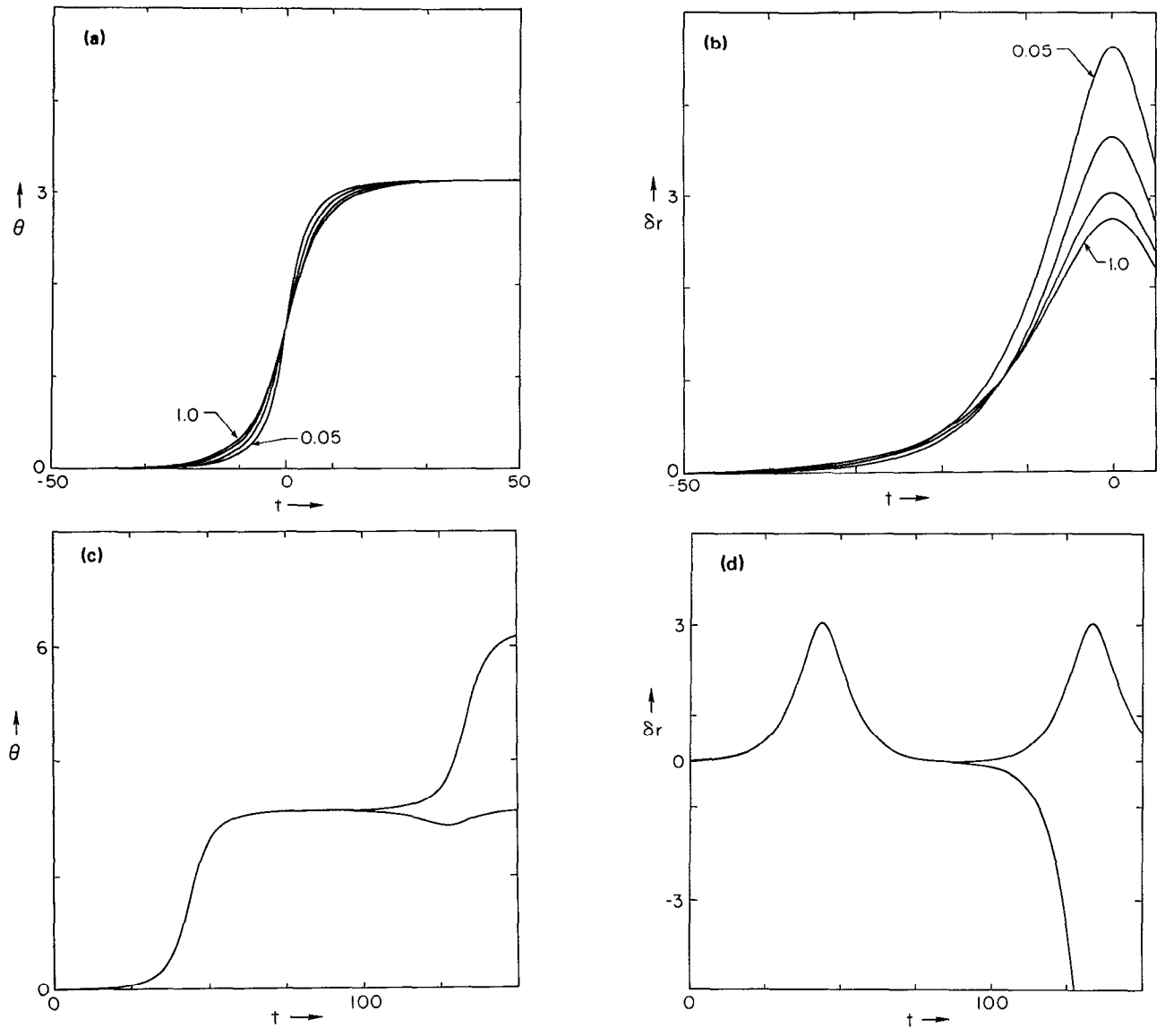

FIG. 18. Nonlinear results of the localized vortex model. (a) $\theta(t)$ for $\varepsilon = 0.05, 0.30, 0.70$, and 1.0. (b) $\delta r(t)$ for the same ε values. (c) Plots of $\theta(t)$ that show trajectories with initial conditions on the two sides of the separatrix. (d) $\delta r(t)$ for two initial conditions, one just inside and the other just outside the separatrix.

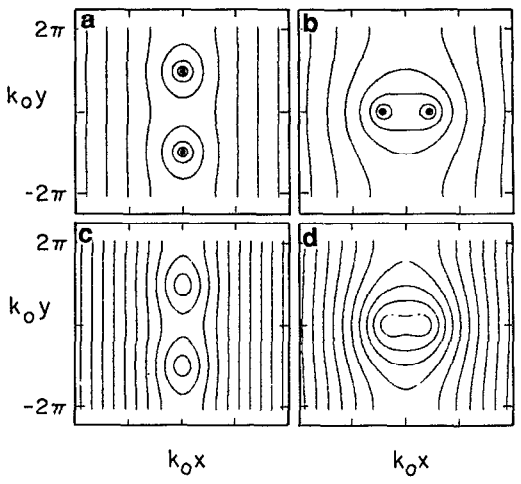

FIG. 19. The streamfunction for the cases: (a) $\phi(x,y,0;1)$, (b) $\phi(x,y,\hat{t};1)$, (c) $\phi(x,y,0;0.6)$, and (d) $\phi(x,y,\bar{t};0.6)$. Here $\hat{t}$ and $\bar{t}$ are chosen so that the rotation is approximately 180°.

resistive plasma with a substantial change in density and perpendicular $E \times B$ flow velocity is given in terms of the transcendental dispersion relation in Sec. II. The roots of the dispersion relations in the absence of shear flow describe the resistive g instability and the collisional drift wave instability with their different dependence on collisionality and magnetic shear. In the presence of a sheared flow, the growth rates are strongly affected when the condition $k_y \Delta x u' > \gamma_k$ is satisfied, where k_y, Δx, and γ_{k_y} are the parameters of the instability in the absence of the shear flow. The critical shear flow u' obtained from this condition is shown in Table I.

For the shear flows reported in the TEXT tokamak plasma with the new higher resolution probe measurements the condition given previously is marginally satisfied so that we conclude that shear flow may have an influence on the edge turbulence, even if it is not sufficiently strong to excite the K–H instability in that experiment.

There are two effects of the sheared $E \times B$ flow on the

edge turbulence. Here, as in Ref. 1, we consider the direct effect of the shear flow on the wave dispersion relation, showing that the growth rate of the mode present in the absence of shear flow can be strongly reduced. The second aspect is that even for a given fixed level of background waves the transport across the magnetic field is reduced by the shear flow. This decorrelation effect of the transport has been calculated by Shaing and Crume[9] and Biglari *et al.*[10] using the ideas of relative diffusion or clump turbulence theory. A simpler estimate of the reduction of the transport comes from considering the single-particle motion of test particles in a dominant fluctuation of mode number k and strength $\tilde{\phi}_k$; the radial excursion size is reduced from the distance π/k_x between nodes of the radial modes to the size $\Delta r = (c\tilde{\phi}_k/Bu')^{1/2}$ given by the strength of the shear flow u' and the amplitude of the potential fluctuation. Taylor *et al.*,[8] Shaing and Crume,[9] Biglari *et al.*,[10] and Burrell *et al.*[7] argue that the reduction in the plasma transport associated with L to H mode transition occurs as a result of the increased sheared flow velocity resulting from the deepening of the negative electrostatic potential well of the toroidal system. We show here how the increased strength of the shear flow changes the stability conditions of the plasma.

We consider the unstable sheared flow regime with implicit particle simulations and describe the resulting vortex dynamics by the motions of the vortex cores. To make an analytic treatment of the vortex core dynamics, we idealize to the case of point vortex dynamics, including the vortex–vortex interactions and the vortex-shear flow dynamics. This appears to give a good description of the principal processes of mutual rotations and coalescence of the vortices. Comparison with the simulations shows that a lowest-order description of the turbulence follows from the vortex core dynamics with treating the density and pressure fields as passively convected. The possibility of describing the relationship of the density and potential fluctuations measured in TEXT with the density being passively convected in the $E \times B$ flows given by the potential fluctuations has been previously suggested by Bengtson and Rhodes.[27]

Previous attempts to explain edge turbulence in TEXT by resistive hydrodynamic modes and by collisional modes have not been completely successful. The theoretical formulas used have neglected the effects of shear flow assuming that the background velocity simply Doppler shifted the frequencies of these instabilities. In view of the present theory and new measurements of Ritz *et al.*[28] (reporting $dv_\theta/dr \leqslant 10^6$/sec, a reexamination of the comparison between fluctuation theory and experiment is necessary, taking into account the finite value of dv_θ/dr. Here the first results of the drift wave resistive g turbulence in the presence of strong shear flow are given for slab approximation to toroidal confinement systems.

ACKNOWLEDGMENTS

The authors thank Dr. E. Solano and members of the Edge Physics Study Group of the IFS for useful discussion.

This research was supported by U.S. Department of Energy Contract No. DE-FG05-80ET-53088. The work was also supported by Joint Institute for Fusion Theory and National Science Foundation Grant No. ATM88-11128.

[1] J. Liu, W. Horton, and J. E. Sedlak, Phys. Fluids **30**, 467 (1987); W. Horton and J. Liu, Phys. Fluids **27**, 2067 (1984).
[2] K. C. Shaing, E. C. Crume, and W. A. Houlberg, Phys. Fluids B **2**, 1492 (1990).
[3] H. Takabe, L. Montierth, and R. L. Morse, Phys. Fluids **26**, 2299 (1983).
[4] H. Takabe, K. Mima, L. Montierth, and R. L. Morse, Phys. Fluids **28**, 3676 (1985).
[5] W. Horton, T. Tajima, and T. Kamimura, Phys. Fluids **30**, 3485 (1987).
[6] R. J. Groebner, P. Gohil, K. H. Burrell, T. H. Osborne, R. P. Seraydarian, and H. St. John, in *Proceedings of the 16th European Conference on Controlled Fusion and Plasma Physics*, Budapest, Hungary (European Physical Society, Geneva, 1989), Vol. I, p. 245.
[7] K. H. Burrell, T. N. Carlstrom, E. J. Doyle, P. Gohil, R. J. Groebner, T. Lehecka, N. C. Luhmann, Jr., H. Matsumoto, T. H. Osborne, W. A. Peebles, and R. Philipona, Phys. Fluids B **2**, 1405 (1990).
[8] R. J. Taylor, M. L. Brown, B. D. Fried, H. Grote, J. R. Liberati, G. J. Morales, P. Pribyl, D. Darrow, and M. Ono, Phys. Rev. Lett. **63**, 2365 (1989).
[9] K. C. Shaing and E. C. Crume, Jr., Phys. Rev. Lett. **63**, 2369 (1989).
[10] H. Biglari, P. H. Diamond, and P. W. Terry, Phys. Fluids B **2**, 1 (1990).
[11] K. Theilhaber and C. K. Birdsall, Phys. Rev. Lett. **62**, 772 (1989); Phys. Fluids B **1**, 2244 (1989).
[12] J. S. Wagner, R. D. Sydora, T. Tajima, T. Hallinan, L. C. Lee, and S. I. Akasofu, J. Geophys. Res. **88**, 8013 (1983).
[13] J. L. Burch, Rev. Space Sci. Space Phys. **21**, 463 (1983).
[14] T. Tajima and J. N. Leboeuf, Phys. Fluids **23**, 884 (1980).
[15] Ch. P. Ritz, R. D. Bengtson, S. J. Levinson, and E. J. Powers, Phys. Fluids **27**, 2956 (1984).
[16] D. C. Barnes, T. Kamimura, J. N. Leboeuf, and T. Tajima, J. Comput. Phys. **52**, 480 (1983).
[17] T. Tajima, *Computational Plasma Physics* (Addison–Wesley, Redwood City, CA, 1989).
[18] A. B. Mikhailovski, in *Theory of Plasma Instabilities* (Plenum, New York, 1974), Vol. 2.
[19] M. N. Rosenbluth and A. Simon, Phys. Fluids **8**, 1300 (1965).
[20] A. Hasegawa and M. Wakatani, Phys. Rev. Lett. **50**, 682 (1983); M. Wakatani and A. Hasegawa, Phys. Fluids **27**, 611 (1984).
[21] P. W. Terry and W. Horton, Phys. Fluids **25**, 491 (1982); **26**, 106 (1983).
[22] S. Chandrasekhar, *Hydrodynamic and Hydromagnetic Stability* (Dover, New York, 1961), Chap. 11.
[23] P. G. Drazin and L. N. Howard, J. Fluid Mech. **14**, 257 (1962).
[24] J. T. Stuart, J. Fluid Mech. **29**, 417 (1967).
[25] R. T. Pierrehumbert and S. E. Windall, J. Fluid Mech. **114**, 59 (1982).
[26] H. Lamb, *Hydrodynamics* (Dover, New York, 1945), 6th ed. p. 225.
[27] R. Bengtson and T. Rhodes (private communication).
[28] Ch. P. Ritz, H. Lin, T. L. Rhodes, and A. J. Wootton, Phys. Rev. Lett. **65**, 2543 (1990).